Noncollinear antiferromagnetic order and effect of spin-orbit coupling in spin-1 honeycomb lattice

Shuyi Li [1], Manh Duc Le,[2] Vaideesh Loganathan,[1] and Andriy H. Nevidomskyy[1,*]

[1]*Department of Physics and Astronomy, Rice University, Houston, Texas 77005, USA*

[2]*ISIS Neutron and Muon Source, Rutherford Appleton Laboratory, Chilton, Didcot OX11 0QX, United Kingdom*

Motivated by the recently synthesized insulating nickelate $Ni_2Mo_3O_8$, which has been reported to have an unusual noncollinear magnetic order of Ni^{2+} $S = 1$ moments with a nontrivial angle between adjacent spins, we construct an effective spin-1 model on the honeycomb lattice, with the exchange parameters determined with the help of first-principles electronic-structure calculations. The resulting bilinear-biquadratic model, supplemented with the realistic crystal-field induced anisotropy, favors the collinear Néel state. We find that the crucial key to explaining the observed noncollinear spin structure is the inclusion of the Dzyaloshinskii–Moriya (DM) interaction between the neighboring spins. By performing variational mean-field and linear spin-wave theory (LSWT) calculations, we determine that a realistic value of the DM interaction $D \approx 2.78$ meV is sufficient to quantitatively explain the observed angle between the neighboring spins. We furthermore compute the spectrum of magnetic excitations within the LSWT and random-phase approximation, which should be compared to future inelastic neutron measurements.

I. INTRODUCTION

Recent experimental and theoretical advances in frustrated magnetism, in particular, the realization of the Kitaev–Heisenberg model [1,2] in the honeycomb lattice materials Na_2IrO_3 [3], Li_2IrO_3 [4], α-$RuCl_3$ [5], and $H_3LiIr_2O_6$ [6] have sparked much interest in the study of quantum magnets with the honeycomb lattice structure. By comparison, honeycomb materials with spin-1 moments have received relatively little attention. Arguably, a larger value of spin makes it more amenable to a semiclassical description, although quantum effects are undeniably important to understand, for instance, the gapped nature of the Haldane ground state in spin-1 chains [7,8]. At the same time, the effect of orbital degrees of freedom and spin-orbit interactions can lead to complex phenomena and a lack of long-range magnetic ordering in spin-1 materials, such as in a recently reported diamond-lattice system $NiRh_2O_4$ [9]. In the case of honeycomb spin-1 materials, the same mechanism that was identified as a source of compasslike Kitaev interactions [2] can result in potentially rich physics, including perhaps spin-liquid ground states. In this paper, we set ourselves a less ambitious task and focus on elucidating the puzzling nature of the noncollinear ground state reported recently in a layered honeycomb lattice oxide $Ni_2Mo_3O_8$ [10], as shown in Fig. 1. While specific to this material, the present paper has wider ramifications for the interplay of frustrations and spin-orbit coupling (SOC) in spin-1 systems.

Most of the known spin-1 honeycomb lattice materials are comprised of Ni^{2+} ions, with the strong Hund's coupling leading to spin $S = 1$ on each site. Similar to the spin-

1/2 case, the vast majority of honeycomb lattice materials, such as $A_3Ni_2SbO_6$ (A = Li, Na) [11], $Na_3Ni_2BiO_6$ [12], and $Li_3Ni_2BiO_6$ [13] order in the zigzag pattern depicted in Fig. 2(f). The Néel order shown in Fig. 2(d) is also possible, as realized, for instance, in $BaNi_2V_2O_8$ [14], while the stripe order is very rare, so far only observed in $Ba_2Ni(PO_4)_2$, where it is argued to be due to a strong interlayer exchange coupling [15,16]. In all the aforementioned cases, the reported magnetic order is collinear, in stark contrast to the material studied here, $Ni_2Mo_3O_8$, which was reported [10] to have a noncollinear magnetic structure depicted schematically in Fig. 1. It is also qualitatively different from other molybdenum oxides with the same hexagonal space group such as $Fe_2Mo_3O_8$ and $Mn_2Mo_3O_8$, which realize either a collinear antiferromagnetic or a ferrimagnetic state [17–19].

In this paper, we show that the key to understanding the noncollinear nature of the magnetic ordering in $Ni_2Mo_3O_8$ is the Dzyaloshinskii–Moriya (DM) interaction that arises due to SOC [20–23]. From the symmetry analysis, the DM vectors are uniquely determined by the Moriya rules [21]. In combination with the exchange couplings computed from first-principles density functional theory (DFT), this allows us to reproduce the experimentally reported magnetic structure. We further compute the generalized phase diagram, with the angle between the two neighboring spins being a function of the DM interaction strength and exchange parameters of the model. Importantly, inclusion of the biquadratic spin-spin interactions of the type $(\vec{S}_i \cdot \vec{S}_j)^2$ is necessary to both fit the *ab initio* results and predict the correct noncollinear magnetic structure.

The remainder of this paper is organized as follows. We present an effective spin-1 model in Sec. II, analyzing the single-ion spin anisotropy term using crystal-field theory in Sec. III. Various competing spin configurations and their
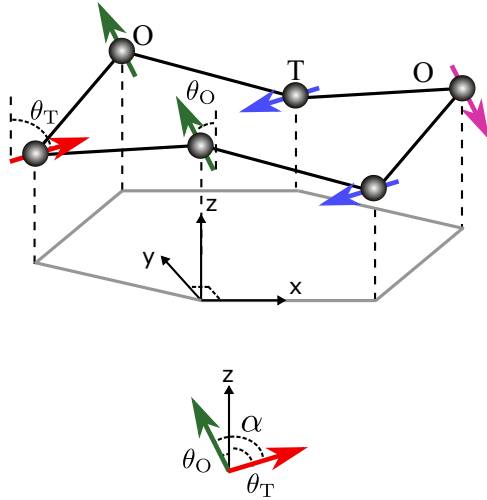
*nevidomskyy@rice.edu

FIG. 1. Depiction of the NCAF state in $Ni_2Mo_3O_8$ [10]. The Ni^{2+} ions are represented by grey spheres. The coordinate system is set up by projecting from the noncentrosymmetric buckled honeycomb lattice onto a regular hexagon in the *ab* plane (marked by light grey color). The two inequivalent Ni sites have either a tetrahedral (*T*) or octahedral (*O*) oxygen coordination. On each of these two sublattices, the spins form a collinear antiferromagnetic order with magnetic ordering wave vector $\vec{q}_m = (\frac{2\pi}{3a}, 0)$, where *a* is the side length of the projected regular hexagon in *xy* plane. When moments lie in the *xz* plane, as is the case in $Ni_2Mo_3O_8$ [10], the angle between the nearby *T* and *O* sites is $\alpha = \theta_T + \theta_O$, as depicted in the lower panel.

mean-field (MF) energies are introduced in Secs. IV and V, followed by the details of determination of spin exchange couplings from *ab initio* calculations in Sec. VI. In Sec. VII, we compute the phase diagram of the model with and without DM interactions, demonstrating that the latter are crucial to reproduce the experimentally reported noncollinear magnetic state. Then, in Sec. VIII, we perform linear spin wave theory (LSWT) calculations in competing phases to capture the quantum fluctuations around MF solutions. Finally, we conclude with the discussion and outlook in Sec. IX.

II. MODEL

$Ni_2Mo_3O_8$ crystallizes in the layered structure characterized by the noncentrosymmetric hexagonal space group $P6_3mc$ [10], with the Ni^{2+} magnetic ions forming a buckled hexagonal structure in each layer shown schematically in Fig. 1. There are two inequivalent Ni sites in this bipartite structure, with alternating atoms having either octahedral or tetrahedral coordination by oxygen ions. The magnetic moments on these two sublattices form two interpenetrating triangular lattices, with an angle α with each other, as depicted in Fig. 1, resulting in a noncollinear antiferromagnetic (NCAF) order.

To model the spin-1 moments on Ni^{2+} ($3d^8$) ions in this material, we adopt a bilinear-biquadratic spin-1 quantum Heisenberg model, first without taking spin-orbit coupling
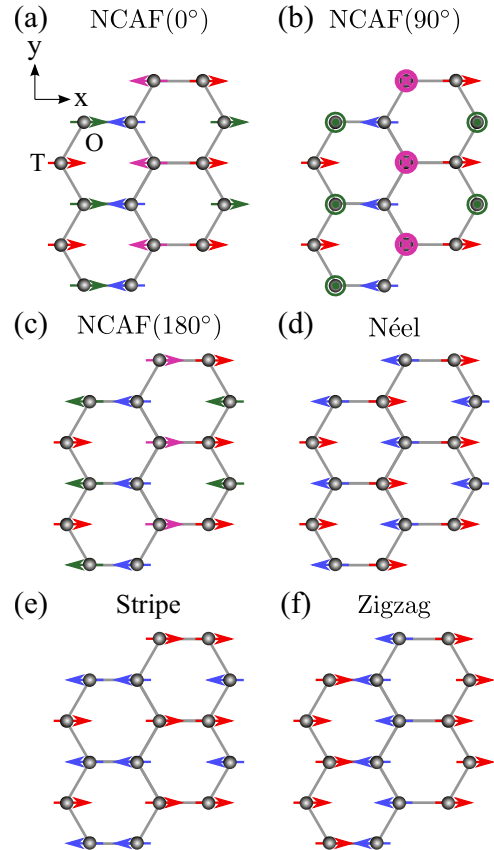

FIG. 2. The depiction of the noncollinear antiferromagnet configuration with (a) $\alpha = 0$, (b) $\alpha = 90°$, and (c) $\alpha = 180°$, with α defined as the angle between the nearest-neighbor spins at *T* site (red) and *O* site (green). Also shown are typical collinear configurations on the honeycomb lattice: (d) Néel state, (e) stripe state, and (f) zigzag state.

into account:

$$
\begin{aligned}
\mathcal{H}_{\text{eff}} = &\sum_{\langle ij \rangle} J_1 \vec{S}_i \cdot \vec{S}_j + K_1 (\vec{S}_i \cdot \vec{S}_j)^2 \\
&+ \sum_{\langle\langle ij \rangle\rangle, T} J_{2T} \vec{S}_i \cdot \vec{S}_j + K_{2T} (\vec{S}_i \cdot \vec{S}_j)^2 \\
&+ \sum_{\langle\langle ij \rangle\rangle, O} J_{2O} \vec{S}_i \cdot \vec{S}_j + K_{2O} (\vec{S}_i \cdot \vec{S}_j)^2 + \mathcal{H}_A,
\end{aligned} \tag{1}
$$

where J_1, K_1 are the nearest-neighbor Heisenberg and biquadratic couplings, while J_{2T}, K_{2T} (J_{2O}, K_{2O}) describe the second-neighbor spin-spin interactions between tetrahedral (octahedral) sites, respectively. As we shall show below in Sec. VI, the inclusion of biquadratic spin-spin interactions is crucial to correctly reproduce the magnon excitation spectrum and to match the energy differences between the various magnetically ordered reference states obtained from *ab initio* calculations. We also take into account the different crystal-field effects on the tetrahedrally and octahedrally coordinated Ni ions, which results in the effective single-ion spin anisotropy Hamiltonian $\mathcal{H}_A$. We shall discuss the form of $\mathcal{H}_A$ in Sec. III below and in Appendix E.

As mentioned earlier, the inclusion of the SOC in the form of the DM interactions among the spins is essential to reproduce the noncollinear magnetic structure. This will be discussed in detail in Sec. VII, here we write the DM Hamiltonian for completeness,

$$\mathcal{H}_{\mathrm{DM}} = \frac{1}{2} \sum_{ij} \vec{D}_{ij} \cdot (\vec{S}_i \times \vec{S}_j), \qquad (2)$$

where $\vec{D}_{ij}$ is a vector whose direction can be determined by Moriya's rules [21], to be discussed in Sec. VII.

III. SINGLE-ION CRYSTAL FIELD ANALYSIS

Due to the interplay of SOC and crystal-field effects on Ni ions, there are single-ion spin anisotropy terms in the Hamiltonian. Because of the threefold rotation symmetry C_3 in the $P6_3mc$ space group, the crystal-field Hamiltonian under Wybourne normalization is given by (see Appendix F for more details)

$$\mathcal{H}_{\mathrm{cf}} = L_{20}\theta_2 \hat{T}_{20} + L_{40}\theta_4 \hat{T}_{40} + L_{43}\theta_4 \hat{T}_{43}, \qquad (3)$$

where L_{lm} are the crystal-field parameters, θ_l are the Stevens factors, and $\hat{T}_{lm}$ are tensorial Stevens–Wybourne operators. We use the point-charge model as discussed in Appendix E which yields the following crystal field parameters:

$$L_{20}^T = +626\,\mathrm{meV}, \quad L_{40}^T = +307\,\mathrm{meV}, \quad L_{43}^T = +764\,\mathrm{meV},$$
$$L_{20}^O = -166\,\mathrm{meV}, \quad L_{40}^O = -1392\,\mathrm{meV}, \quad L_{43}^O = 1623\,\mathrm{meV}.$$
$$(4)$$

While the Hamiltonian Eq. (3) acts on the components of the orbital momentum, the spin degrees of freedom feel the effect of anisotropies because of the SOC $\lambda \vec{S} \cdot \vec{L}$. Estimating the coupling constant $\lambda \approx -40$ meV [24], as is typical for Ni ions, we treat it as a perturbation. While the first order of the perturbation vanishes identically, the correction to the energy in the second-order perturbation theory is of the form

$$E_{\mathrm{2nd}} = \lambda^2 \sum_{i,j} \Lambda_{ij} S^i S^j. \qquad (5)$$

This results in the effective single-ion spin anisotropy Hamiltonian

$$\mathcal{H}_{\mathrm{A}} = \sum_T \gamma_T (S_i^z)^2 + \sum_O \gamma_O (S_i^z)^2, \qquad (6)$$

with $\gamma_T = 30.41$ meV, $\gamma_O = -0.53$ meV (see Appendix F for details of the derivation). The above equation would predict the lowest energy singlet on the tetrahedral site, with the higher-lying doublet at energy γ_T, however further corrections in the 4th and higher orders perturbation theory (see Appendix F) lower the crystal field energy splitting down to $\gamma_T \approx 17$ meV. While the value of the single ion anisotropy γ_O we obtained is negative, i.e. favors a doublet on the octahedral site, it should be noted that a small positive value of γ_O, favouring the $S^z = 0$ singlet, fits the INS data equally well. These values imply the tetrahedral sites strongly prefer to lie in the xy plane, while the octahedral sites a have weak preference to align along z.

IV. SPIN CONFIGURATIONS

In $Ni_2Mo_3O_8$, the state we are mainly interested in is the NCAF state shown in Fig. 1. The neutron scattering analysis [10] shows that the moments form a coplanar structure in the xz plane, with the x axis pointing along one of the hexagonal bonds and the z axis being the hexagonal c axis of the crystal, as indicated in Fig. 1. In the honeycomb lattice, the tetrahedral (T) and octahedral (O) sites form two interpenetrating triangular sublattices. To completely characterize various spin states, we introduce the polar angles θ_T and θ_O relative to the z axis on each sublattice and the azimuthal angles ϕ_T and ϕ_O with the x axis, respectively. The angle α between the neighboring spins on the two sublattices is then given by

$$\cos\alpha = \sin\theta_T \sin\theta_O \cos(\phi_T - \phi_O) + \cos\theta_T \cos\theta_O. \quad (7)$$

Since the moments in the experimental NCAF phase lie in the xz plane, the azimuthal angles are either 0 or π, and moreover $|\phi_T - \phi_O| = \pi$. Furthermore, it is confirmed by the numerical result from classical energy minimization, which is shown in Appendix D. We shall therefore take this to be the case in the following. From Eq. (7), it then follows that the angle α between the two spins is

$$\alpha = \theta_T + \theta_O, \qquad (8)$$

as depicted in the bottom of Fig. 1. For convenience, if $\alpha > 180°$, it is equivalent to use $\alpha' = 360° - \alpha$ as the angle between two spin directions. Thus it is sufficient to only consider $0° \leqslant \alpha \leqslant 180°$.

While the experimental ground state of $Ni_2Mo_3O_8$ is noncollinear, it is instructive to look at the various collinear magnetic orders obtained by setting $\alpha = 0$ or $\alpha = 180°$, depicted in Figs. 2(a) and 2(c), respectively. In the honeycomb lattice model, one often considers three important collinear spin ordered states: Néel, stripe, and zigzag states, depicted in Figs. 2(d)–2(f). As the figure illustrates, the zigzag and stripe orders correspond to $\alpha = 0$ and $\alpha = 180°$, respectively, and one can think of noncollinear NCAF states with generic value of α as lying in-between these two limiting cases, such as, for instance, the special case with $\alpha = 90°$ depicted in Fig. 2(b).

We note that the experimental study in Ref. [10] reports two possible magnetic structures, with different sizes and directions of the magnetic moments; which we summarize in Table I. Both structures provide an equally good fit to the neutron scattering refinements, however, as we shall show below, our theoretical analysis suggests that the experimental structure 1, with $\alpha' = 130°$, is most likely realized in $Ni_2Mo_3O_8$.

V. MEAN-FIELD ENERGY OF DIFFERENT MAGNETIC ORDERS

Our goal is to obtain accurate estimates of the exchange couplings in the model Hamiltonian Eq. (1) from first-principles calculations. To do this, we first evaluate analytically the MF energies of several reference ordered states $|\psi\rangle$, namely, the ferromagnetic (FM), Néel, stripe, and zigzag states, by using spin-1 product states as a MF ansatz,

$$|\psi\rangle = \prod_i \otimes |\vec{S}_i\rangle, \qquad (9)$$

TABLE I. Spin configurations and magnetic moments of the two experimental fits to the neutron scattering data on $Ni_2Mo_3O_8$, inferred from Ref. [10]. The angles θ and ϕ for the two sublattices are defined in the text.

	θ_T	ϕ_T	M_T	θ_O	ϕ_O	M_O	α	α'
Fit 1	85°	180°	$1.727\mu_B$	145°	0°	$1.431\mu_B$	230°	130°
Fit 2	124°	180°	$1.997\mu_B$	87°	0°	$0.891\mu_B$	211°	149°

where $|\vec{S}_i\rangle$ on a given site is the maximum weight eigenstate (i.e., spin-up eigenstate) of the operator $\hat{\vec{S}}_i \cdot \hat{n}_i$, projecting the spin onto the local direction $\hat{n}_i = (\sin\theta_i \cos\phi_i, \sin\theta_i \sin\phi_i, \cos\theta_i)$. Written explicitly, $|\vec{S}_i\rangle$ is given by a linear superposition

$$|\vec{S}_i\rangle = e^{-i\phi_i}\cos^2\frac{\theta_i}{2}|1\rangle + e^{i\phi_i}\sin^2\frac{\theta_i}{2}|-1\rangle$$
$$+ \sqrt{2}\sin\frac{\theta_i}{2}\cos\frac{\theta_i}{2}|0\rangle. \quad (10)$$

By choosing different local (θ_i, ϕ_i) directions, we can capture different ordered states. For instance, the FM state is given by $[\theta_T = \theta_O, \phi_T = \phi_O]$, whereas the Néel state is accommodated by $[\theta_T = \theta_O + 180°, \phi_T = \phi_O]$. The resulting MF expressions for the energies of the various reference states are as follows:

$$\mathcal{E}_{\mathrm{FM}} = \frac{3}{2}J_1 + \frac{3}{2}J_{2T} + \frac{3}{2}J_{2O}$$
$$+ \frac{\gamma_T}{4}(\cos^2\theta_T + 1) + \frac{\gamma_O}{4}(\cos^2\theta_O + 1),$$

$$\mathcal{E}_{\mathrm{N\acute{e}el}} = -\frac{3}{2}J_1 + \frac{3}{2}K_1 + \frac{3}{2}J_{2T} + \frac{3}{2}J_{2O}$$
$$+ \frac{\gamma_T}{4}(\cos^2\theta_T + 1) + \frac{\gamma_O}{4}(\cos^2\theta_O + 1),$$

$$\mathcal{E}_{\mathrm{stripe}} = -\frac{1}{2}J_1 + K_1 - \frac{1}{2}J_{2T} + K_{2T} - \frac{1}{2}J_{2T} + K_{2O}$$
$$+ \frac{\gamma_T}{4}(\cos^2\theta_T + 1) + \frac{\gamma_O}{4}(\cos^2\theta_O + 1),$$

$$\mathcal{E}_{\mathrm{zigzag}} = \frac{1}{2}J_1 + \frac{1}{2}K_1 - \frac{1}{2}J_{2T} + K_{2T} - \frac{1}{2}J_{2T} + K_{2O}$$
$$+ \frac{\gamma_T}{4}(\cos^2\theta_T + 1) + \frac{\gamma_O}{4}(\cos^2\theta_O + 1). \quad (11)$$

Because Eqs. (11) are linearly dependent, we introduce more reference states to be able to determine the exchange couplings uniquely (see Appendix A for more details). For future reference, we provide here the MF expression for the energy of the NCAF state for an arbitrary angle α between the spins on T and O sites, as defined in Fig. 1 and in Eq. (7):

$$\mathcal{E}_{\mathrm{NCAF}} = \frac{1}{2}J_1\cos\alpha + K_1\left(\frac{3}{8}\cos^2\alpha - \frac{1}{4}\cos\alpha + \frac{3}{8}\right)$$
$$- \frac{1}{2}J_{2T} + K_{2T} - \frac{1}{2}J_{2T} + K_{2O}$$
$$+ \frac{\gamma_T}{4}(\cos^2\theta_T + 1) + \frac{\gamma_O}{4}(\cos^2\theta_O + 1). \quad (12)$$

VI. DFT ANALYSIS

We have performed *ab initio* DFT calculations on $Ni_2Mo_3O_8$ (see Appendix B for details) in various spin-

ordered states, both collinear and noncollinear, and computed the corresponding energies. By fixing a collinear ordered state and choosing different *global* rotations, we have found that DFT captures the single-ion anisotropy (SIA) poorly—the resulting energy differences are about 0.1 meV per site, much less than expected from the relatively large value of γ_T in Eq. (6). This is a known effect to do with the inaccuracy of capturing crystal-field splittings and the approximate way in which the SOC is treated in typical *ab initio* codes. Similarly, the Dm interactions are not captured well at the level of DFT. Thus, we used the DFT reference energies to determine only six unknown parameters in Eq. (1): J_1, J_{2T}, J_{2O}, K_1, K_{2T}, and K_{2O}. Substituting these *ab initio* energies into the left-hand side of the MF expressions in Eq. (11) and other reference states (see Appendix A), we use least-squares fitting to determine the set of the exchange coefficients. In total, 12 reference states, and hence 11 energy differences have been used, resulting in the excellent quality of the least-squares fit ($R^2 = 0.956$) shown in Fig. 3. The obtained values of the fitting parameters are as follows:

$$J_1 = +2.62\,\mathrm{meV}, \quad K_1 = -1.13\,\mathrm{meV},$$
$$J_{2T} = +0.35\,\mathrm{meV}, \quad K_{2T} = -0.35\,\mathrm{meV},$$
$$J_{2O} = +0.41\,\mathrm{meV}, \quad K_{2O} = +0.09\,\mathrm{meV}. \quad (13)$$

The most important conclusion for this paper is that the value of K_1 is negative and non-negligible compared to the Heisenberg exchange J_1. The presence of such biquadratic terms in the model Eq. (1) is important to correctly capture the physics of spin-1 interactions, as was proven to be the case in other $3d$ metals with spin-1 moments, notably iron pnictides and chalcogenides. There, one also finds negative and
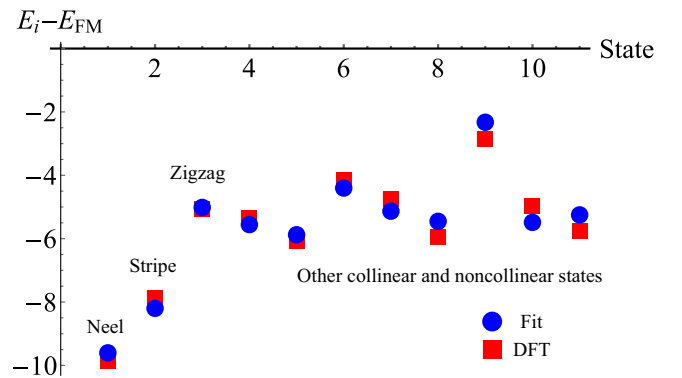

FIG. 3. Least-squares fitting of the mean-field energies for the model in Eq. (1) to the *ab initio* DFT energies for 11 reference magnetically ordered states (relative to the FM state energy). The red points indicate the *ab initio* energies, while the blue points are the MF energy difference with the best fitting parameters quoted in Eq. (13).

relatively large values of K_1 from first-principles calculations [25,26], and it turns out to be essential to correctly describe the magnon dispersion in inelastic neutron scattering [27–30]. In the present case, we shall show that the presence of the K_1 term affects the relative stability of the Néel and noncollinear magnetic states (see Sec. VII B).

The *ab initio* electronic-structure calculations reveal additional information about the magnetic properties of $Ni_2Mo_3O_8$. The magnitude of the magnetic moment remains unchanged across the various ordered states and is dominated by the Hund's coupled spin contribution of $\langle \hat{M}_S \rangle = 1.45\ \mu_B$ per Ni for both types (T, O) of Ni atoms. There is also an orbital moment contribution, which is an order of magnitude smaller, $\langle \hat{M}_L^{(T)} \rangle = 0.18\ \mu_B$ on the tetrahedral Ni ion and $\langle \hat{M}_L^{(O)} \rangle = 0.12\ \mu_B$ on the octahedral ion (the slightly different values are due to the difference in the crystal-field environment on the two sites). The total magnetic moment is thus predicted to be $\langle \hat{M}_J \rangle = \langle \hat{M}_S \rangle + \langle \hat{M}_L \rangle = 1.63\ \mu_B$ on the tetrahedral site and $1.57\ \mu_B$ on the octahedral site. These values of the moments are closer to the first of the two experimental fits from Ref. [10] shown in Table I.

VII. RESULTS

Having estimated the spin-exchange couplings from the *ab initio* calculations and the SIA from a point-charge model (see Sec. III), we now proceed to compute the theoretical phase diagram as a function of these parameters, in two regimes: First without the DM interaction using the effective spin model in Eq. (1), and then incorporating it into the model. As we shall demonstrate, the DM interaction is crucial to correctly capture the NCAF state observed experimentally [10] in $Ni_2Mo_3O_8$.

A. Results without DM interaction

Because γ_T is positive and large in Eq. (6), the moments on tetrahedral sites prefer to lie in the xy plane, consistent with the polar angle θ_T close to $90°$ in the experimental fit 1 in Table I. For the model parameters in Eq. (13), the classical Luttinger-Tisza method and minimization of classical energy show that the ground state has Néel order (see Appendixes C and D for more details). This conclusion is corroborated by the MF calculations—indeed, by comparing the expected energies of the different magnetic states in Eq. (11) and Eq. (12), we find that in the absence of the DM interaction, the collinear Néel phase dominates a large portion of the phase diagram, with both the T and O moments lying in the xy plane. This is illustrated in Fig. 4 [the parameters in Eq. (13) are shown with an asterisk, which lies inside the Néel phase], where we have fixed the values of J_1, J_{2O}, K_{2T}, K_{2O}, γ_T, and γ_O, and show the phase diagram as a function of the relative strength of J_{2T} and K_1. We have set $J_1 > 0$ since both the experiment and our *ab initio* calculations indicate that the nearest-neighbor exchange is antiferromagnetic, see Eq. (13).

Competing with the Néel state is the noncollinear state parametrized by the relative angle $\alpha = \theta_T + \theta_O$ on the two sublattices [see Eq. (7) and Fig. 1 for the meaning of α]. Note that the MF energy of such a noncollinear state $\mathcal{E}_{NCAF}$ in Eq. (12) is a function of θ_T and the relative angle α. We determine the optimal angles α and θ_T by minimizing the
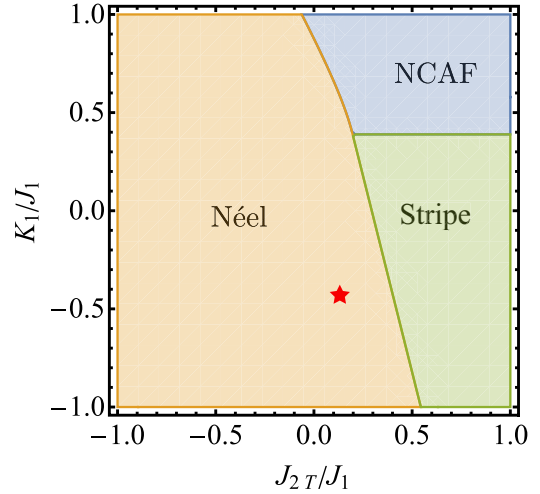

FIG. 4. The phase diagram of the model in Eq. (1) in the ($J_{2T} - K_1$) parameter space. The values $J_1 = 2.62$ meV $J_{2O} = 0.41$ meV, $K_{2T} = -0.35$, and $K_{2O} = 0.09$ meV are fixed as determined from *ab initio* calculations. The red asterisk corresponds to the set of parameters ($J_{2T} = 0.35$ meV, $K_1 = -1.13$ meV) determined from *ab initio* calculations in Eq. (13).

energy $\frac{\partial \mathcal{E}_{NCAF}}{\partial \alpha} = 0$ and $\frac{\partial \mathcal{E}_{NCAF}}{\partial \theta_T} = 0$, which results in a set of coupled equations:

$$\gamma_T \sin 2\theta_T = (-2J_1 - 3K_1 \cos\alpha + K_1)\sin\alpha,$$
$$\gamma_T \sin 2\theta_T = \gamma_O \sin 2(\alpha - \theta_T). \quad (14)$$

Note that the stripe phase shown in Fig. 2(e) is a special case of the NCAF state with $\alpha = \pi$, and we find the stripe state to be stabilized for sufficiently large J_{2T}, provided K_1 is below $\lesssim 0.4 J_1$, as shown in Fig. 4.

Our *ab initio* calculations indicate that K_1 is negative, and the set of exchange parameters computed from DFT (shown with an asterisk in Fig. 4) lies very close to the boundary between the Néel and the stripe phase. It is clear from Fig. 4 that unless the value of K_1 is sufficiently large and positive (namely, $K_1 > 0.39 J_1$), which is not the case in our *ab initio* set of parameters, the noncollinear solution will *not* be realized. The inclusion of quantum fluctuations beyond MF theory does not alter this conclusion, as will be demonstrated below in Sec. VIII. We therefore turn our attention to the effect of DM interactions, which as we show below, qualitatively changes the phase diagram.

B. The effect of DM interaction

As shown above, the Heisenberg model favors collinear spin ordering. The noncentrosymmetric crystal structure of $Ni_2Mo_3O_8$ motivates us to consider DM interactions arising from SOC. While it will not affect the energies of the collinear spin configurations such as the Néel, stripe, or zigzag states, the DM interaction can potentially lower the energy of the noncollinear states.

Consider first the DM interaction between spins on the nearest sites O and T. In a noncentrosymmetric honeycomb lattice, there is only one mirror plane that includes both sites, which is perpendicular to the ab plane. From Moriya's rules,
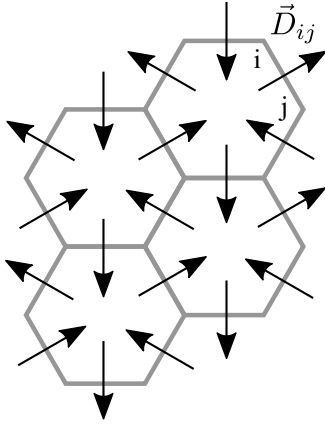
FIG. 5. The DM vectors for nearest-neighboring bonds of non-centrosymmetric honeycomb lattice in xy plane.

the vector $\vec{D}_{OT}$ should be perpendicular to this mirror plane, which means that $\vec{D}_{OT}$ lies in the ab plane, and is perpendicular to the bond direction $\vec{OT}$. By the C_3 rotational symmetry of the lattice, we can obtain the vectors $\vec{D}_{ij}$ for all nearest-neighbor sites, as shown in Fig. 5, which should all have the same magnitude $|\vec{D}_{ij}| = D$.

Before computation of the energy by using spin-1 product states, we first perform the minimization to the classical energy under the model parameters in Eq. (13) (see Appendix D for more details), and it shows that the ground state is in the Néel phase for a small DM strength D, and it becomes NCAF state after D being larger than a critical value $D_C \approx 1.18J_1$. Thus, in the following discussion, we only consider the competition between Néel and NCAF phases, and ignore other states whose classical energies are higher.

At the expected energy level, the average energy per site of the variational NCAF state is

$$\mathcal{E}'_{\text{NCAF}} = \tfrac{1}{2}J_1 \cos\alpha + K_1\left(\tfrac{3}{8}\cos^2\alpha - \tfrac{1}{4}\cos\alpha + \tfrac{15}{8}\right)$$
$$- \tfrac{1}{2}J_{2T} + \tfrac{5}{2}K_{2T} - \tfrac{1}{2}J_{2O} + \tfrac{5}{2}K_{2O}$$
$$- D(\sin\theta_O \cos\phi_O \cos\theta_T - \sin\theta_T \cos\phi_T \cos\theta_O)$$
$$+ \tfrac{1}{4}\gamma_T(\cos^2\theta_T + 1) + \tfrac{1}{4}\gamma_O(\cos^2\theta_O + 1), \quad (15)$$

where, as before, $\alpha = \theta_T + \theta_O$ is the angle between the spins on the tetrahedral and octahedral sites, as indicated in Fig. 1. Under the assumption that both spins lie in the plane containing the O–T bond, as realized in the experiment ($|\phi_T - \phi_O| = \pi$ in our notation), the DM term results in the energy contribution:

$$\mathcal{E}_{\text{DM}} = D\cos\phi_T \sin\alpha. \quad (16)$$

To minimize this energy we choose, without loss of generality, $\phi_T = 180°$, which corresponds to the experimental results in Table I. The energy of the NCAF ordered state then becomes

$$\mathcal{E}'_{\text{NCAF}} = \tfrac{1}{2}J_1 \cos\alpha + K_1\left(\tfrac{3}{8}\cos^2\alpha - \tfrac{1}{4}\cos\alpha + \tfrac{3}{8}\right)$$
$$- \tfrac{1}{2}J_{2T} + K_{2T} - \tfrac{1}{2}J_{2O} + K_{2O} - D\sin\alpha$$
$$+ \tfrac{1}{4}\gamma_T(\cos^2\theta_T + 1) + \tfrac{1}{4}\gamma_O(\cos^2(\alpha - \theta_T) + 1). \quad (17)$$
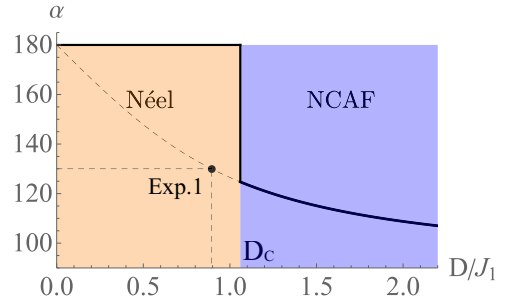

FIG. 6. The optimal value of angle α corresponding to the minimum NCAF energy as a function of DM strength D, with the exchange parameters fixed at the *ab initio* values in Eq. (13). The dashed lines corresponds to the experimental value of $\alpha' = 130°$, achieved at $D \approx 2.35$ meV.

By minimizing this energy with respect to the variational parameter α and θ_T, we thus obtain the optimal value of α for a given D [it is clear from Eq. (17) that it suffices to consider $D > 0$, since $0 \leqslant \alpha \leqslant \pi$]. The resulting optimal angle as a function of the DM interaction strength D is shown in Fig. 6. It shows that for D less than a critical value of $D_c = 1.06J_1 \approx 2.78$ meV, the Néel state is the ground state, and for larger values of the DM interaction, a first-order phase transition into the NCAF state takes place, with angle α jumping to a value $\alpha \lesssim 124.7°$. Note that the critical value of D_c results in the angle close to the experimentally reported $\alpha' = 130°$ in Table I.

So far, we have fixed the exchange parameters of the Hamiltonian to be those from the first-principles calculations in Eq. (13) and only varied the DM interaction strength D. Now, we relax the exchange parameters and investigate the phase diagram as a function of J_{2T}/J_1 and D in Fig. 7(a). We see that the NCAF phase wins over the Néel phase provided J_{2T} is sufficiently large, and the angle α varies continuously within the NCAF phase, shown as a false color in Fig. 7. A similar conclusion is reached when we fix J_{2T} to its *ab initio* value and study the phase diagram as a function of the
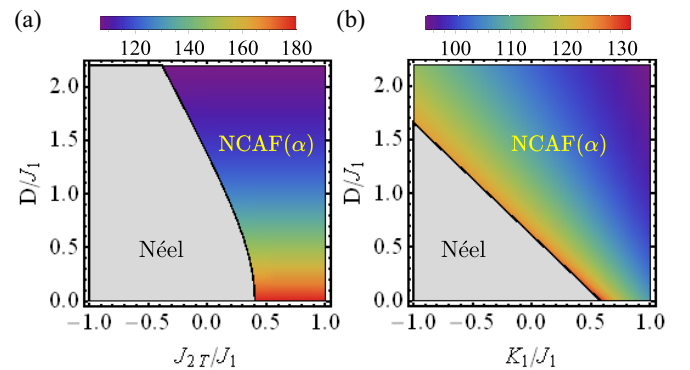

FIG. 7. (a) The phase diagram as a function of parameters D and J_2 with the remaining exchange couplings fixed at the *ab initio* values listed in Eq. (13) and with fixed effective anisotropy parameters ($\gamma_T = 30.41$, $\gamma_O = -0.53$). The false color denotes the optimized value of angle α. (b) The phase diagram as a function of parameters D and K_1, with the remaining exchange couplings fixed at the *ab initio* values in Eq. (13).

biquadratic interaction K_1, plotted in Fig. 7(b). In the latter case, the NCAF phase can be stabilized at an arbitrary value of K_1 (including $K_1 = 0$), provided D is sufficiently large. Conversely, a large value of $K_1 > 0.39J_1$ favors the NCAF phase even in the absence of the DM interaction—the same conclusion reached earlier in Sec. VII A (see Fig. 4).

In Figs. 7(a) and 7(b), the optimized angle α_{opt}, shown as a false color, corresponds to the minimum NCAF energy under given D. This optimal angle decreases from $180°$ [which corresponds to the collinear stripe phase, see Figs. 2(c) and 2(e)] down to $90°$ as D increases, as expected since the larger DM interaction favors the noncollinear ordered state.

VIII. QUANTUM FLUCTUATIONS AROUND MEAN FIELD

In this section, we investigate the effect of quantum fluctuation around the MF solution for the ordered states. We perform LSWT calculations to compute the contribution of the magnon zero-point energy to the Néel and NCAF states, whose competition in $Ni_2Mo_3O_8$ is the principal goal of this paper. Because LSWT can only handle the bilinear spin terms, first we approximate the biquadratic-bilinear model to an effective Heisenberg model, which we then treat at the level of LSWT.

A. Effective Heisenberg model

Unless one is interested in quadrupolar spin ordering, which is not the case in $Ni_2Mo_3O_8$, it is often sufficient to approximate the biquadratic terms $(\vec{S}_i \cdot \vec{S}_j)^2$ by a MF decoupling

$$J\vec{S}_i \cdot \vec{S}_j + K(\vec{S}_i \cdot \vec{S}_j)^2 \approx J_e(\vec{S}_i \cdot \vec{S}_j) - K\langle \vec{S}_i \cdot \vec{S}_j \rangle^2, \quad (18)$$

whereby one obtains an effective Heisenberg model with an effective spin exchange $J_e = J + 2K\langle \vec{S}_i \cdot \vec{S}_j \rangle$. However, this does not work well in the case of noncollinear ordering because the MF energy of the right-hand side in Eq. (18),

$$\langle J_e(\vec{S}_i \cdot \vec{S}_j) - K\langle \vec{S}_i \cdot \vec{S}_j \rangle^2 \rangle = J\cos\alpha_{ij} + K\cos^2\alpha_{ij}, \quad (19)$$

is far from the expectation value of the energy of the left-hand side computed quantum-mechanically for spin-1 objects,

$$\langle J\vec{S}_i \cdot \vec{S}_j + K(\vec{S}_i \cdot \vec{S}_j)^2 \rangle$$
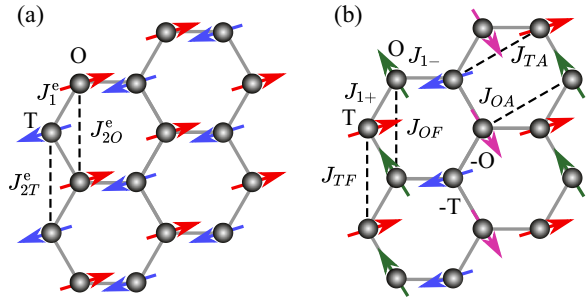$$= \left(J - \frac{K}{2}\right)\cos\alpha_{ij} + \frac{K}{4}\cos^2\alpha_{ij} + \frac{5}{4}K, \quad (20)$$

FIG. 8. The depiction of the effective Heisenberg model for (a) Néel state and (b) NCAF state. The spins in the sketch of NCAF state are used for showing the effective model clearly, however, we should notice that the spins of NCAF state are in xz plane.

except for when the two spins are alligned ferromagnetically ($\alpha_{ij} = 0$).

Instead, we approximate the spin-spin interaction as

$$J\vec{S}_i \cdot \vec{S}_j + K(\vec{S}_i \cdot \vec{S}_j)^2 \approx J_e(\vec{S}_i \cdot \vec{S}_j) - K\langle \vec{S}_i \cdot \vec{S}_j \rangle^2 + f(K), \quad (21)$$

with a constant $f(K)$ to be determined by requiring that the expectation values of the energy on the two sides of the above equation are equal:

$$J_e\langle \vec{S}_i \cdot \vec{S}_j \rangle - K\langle \vec{S}_i \cdot \vec{S}_j \rangle^2 + f(K) = \langle J\vec{S}_i \cdot \vec{S}_j + K(\vec{S}_i \cdot \vec{S}_j)^2 \rangle. \quad (22)$$

This yields an *effective* Heisenberg exchange coupling

$$J_e(\alpha_{ij}) = J + \left(\frac{5}{4}\cos\alpha_{ij} - \frac{1}{2}\right)K \quad (23)$$

and $f(K) = 5/4K$. Notice that the parameters of the resulting model explicitly depend on the angle α_{ij} between the spins in the ordered state. For example, for the Néel state shown in Fig. 8(a), the effective model reads

$$\mathcal{H}_{\text{Néel}}^{\text{e-int}} = \sum_{\langle ij \rangle} J_1^e \vec{S}_i \cdot \vec{S}_j + \sum_{\langle\langle ij \rangle\rangle, T} J_{2T}^e \vec{S}_i \cdot \vec{S}_j + \sum_{\langle\langle ij \rangle\rangle, O} J_{2O}^e \vec{S}_i \cdot \vec{S}_j, \quad (24)$$

with the effective coupling constants given by

$$J_1^e = J_1 - \frac{7}{4}K_1, \quad J_{2T}^e = J_{2T} + \frac{3}{4}K_{2T}, \quad J_{2O}^e = J_{2O} + \frac{3}{4}K_{2O}. \quad (25)$$

Similarly, the effective spin-bilinear Hamiltonian for the NCAF state shown in Fig. 8(b) takes the form

$$\mathcal{H}_{\text{NCAF}}^{\text{e-int}} = \sum_{\langle T,O \rangle, \langle -T,-O \rangle} J_{1+}\vec{S}_i \cdot \vec{S}_j + \sum_{\langle T,-O \rangle, \langle O,-T \rangle} J_{1-}\vec{S}_i \cdot \vec{S}_j + \sum_{\langle\langle T,T \rangle\rangle} J_{TF}\vec{S}_i \cdot \vec{S}_j + \sum_{\langle\langle -T,-T \rangle\rangle} J_{TF}\vec{S}_i \cdot \vec{S}_j$$
$$+ \sum_{\langle\langle T,-T \rangle\rangle} J_{TA}\vec{S}_i \cdot \vec{S}_j + \sum_{\langle\langle O,O \rangle\rangle} J_{OF}\vec{S}_i \cdot \vec{S}_j + \sum_{\langle\langle -O,-O \rangle\rangle} J_{OF}\vec{S}_i \cdot \vec{S}_j + \sum_{\langle\langle O,-O \rangle\rangle} J_{OA}\vec{S}_i \cdot \vec{S}_j, + \sum_{\langle ij \rangle} \vec{D}_{ij} \cdot (\vec{S}_i \times \vec{S}_j), \quad (26)$$

where $-T$ corresponds to the tetrahedral sites with the spin direction $(\theta_T + \pi, \phi_T)$ [denoted by blue arrows in Fig. 8(b)] and $-O$ denotes the octahedral site with the spin pointing along $(\theta_O + \pi, \phi_O)$ [denoted by magenta arrows in Fig. 8(b)]. Thus, the price paid for writing the effective Heisenberg model is that the effective spin exchange couplings become anisotropic. The total number of effective coupling constants thus increases from three to six, compared to the Néel state, with the values given by

$$J_{1+}(\theta_T, \theta_O) = J_1 + K_1\left(\frac{5}{4}\cos(\theta_T + \theta_O) - \frac{1}{2}\right),$$
$$J_{1-}(\theta_T, \theta_O) = J_1 + K_1\left(-\frac{5}{4}\cos(\theta_T + \theta_O) - \frac{1}{2}\right),$$

$$J_{TF} = J_T + \tfrac{3}{4}K_T, \quad J_{TA} = J_T - \tfrac{7}{4}K_T,$$

$$J_{OF} = J_O + \tfrac{3}{4}K_O, \quad J_{OA} = J_O - \tfrac{7}{4}K_O. \quad (27)$$

B. Linear spin wave theory

Since the LSWT is the large-S expansion around the ordered state, it is convenient to choose the local spin quantization axis z_i on each site along the direction of the spin in the given state. In this local frame, the Holstein–Primakoff (HP) transformation of the spin operators is given by the standard expressions

$$s_i^+ = \sqrt{2S}b, \quad s_i^- = \sqrt{2S}b^\dagger, \quad s_i^z = S - b^\dagger b. \quad (28)$$

The original spin operators S_i in the laboratory frame are related to these local spin operators s_i by a rotation in the xz plane as follows:

$$S_i^x = \cos\theta_i\, s_i^x - \sin\theta_i\, s_i^z, \quad S_i^y = s_i^y,$$

$$S_i^z = \sin\theta_i\, s_{i0}^x + \cos\theta_i\, s_i^z. \quad (29)$$

The Heisenberg interaction, expressed in terms of the HP bosons, thus becomes

$$\vec{S}_i \cdot \vec{S}_j = S^2 \cos\alpha_{ij} - S \cos\alpha_{ij}(b_i^\dagger b_i + b_j^\dagger b_j)$$

$$+ \frac{S}{2}(1 + \cos\alpha_{ij})(b_i^\dagger b_j + b_i b_j + \text{H.c.})$$

$$+ \sqrt{\frac{S}{2}} \sin\alpha_{ij}(b_i - b_j + \text{H.c.}), \quad (30)$$

and similarly for the DM interaction. After HP transformation, the effective Hamiltonian in momentum space can be written as

$$\mathcal{H} = \mathcal{E}_0 + \mathcal{E}_C + H_{\text{lin}}[b^\dagger, b] + \sum_{\vec{k}} \psi_{\vec{k}}^\dagger H(\vec{k}) \psi_{\vec{k}}, \quad (31)$$

where $\mathcal{E}_0$ is the MF energy, $\mathcal{E}_C$ is the term from commutation relation when we construct bosonic Nambu representation written in terms of $\psi_{\vec{k}} = [b_{T,\vec{k}}, b_{O,\vec{k}}, b_{T,-\vec{k}}^\dagger, b_{O,-\vec{k}}^\dagger]^{\mathsf{T}}$, where b_T and b_O are annihilation operators at T and O sites, respectively. The explicit form of the matrix $H(\vec{k})$ is shown in Appendix G. Above, H_{lin} is the part of the Hamiltonian linear in the boson creation/annihilation operators, which we ignore as it does not conserve the number of bosons (magnons). Physically, this term appears when the reference magnetic state is not the saddle point of the Hamiltonian, which may happen in the NCAF state for technical reasons to do with approximating the biquadratic spin interaction via an effective Heisenberg term.

The last term in Eq. (31), after the Bogoliubov transformation, becomes diagonal in the Bogoliubov operator basis, resulting in the zero-point fluctuation contribution to the energy of an ordered state,

$$\mathcal{E}_{\text{LSW}} = \mathcal{E}_0 + \mathcal{E}_C + \frac{3\sqrt{3}}{4(2\pi)^2} \sum_i \sum_{\vec{k} \in \text{BZ}} E_i(\vec{k}), \quad (32)$$

where $E_i(\vec{k})$ labels the positive eigenenergies of $H(\vec{k})$ and the sum is over all the magnon bands. We perform the linear spin wave calculation for the two competing states: Néel and NCAF, see Appendix G for details.
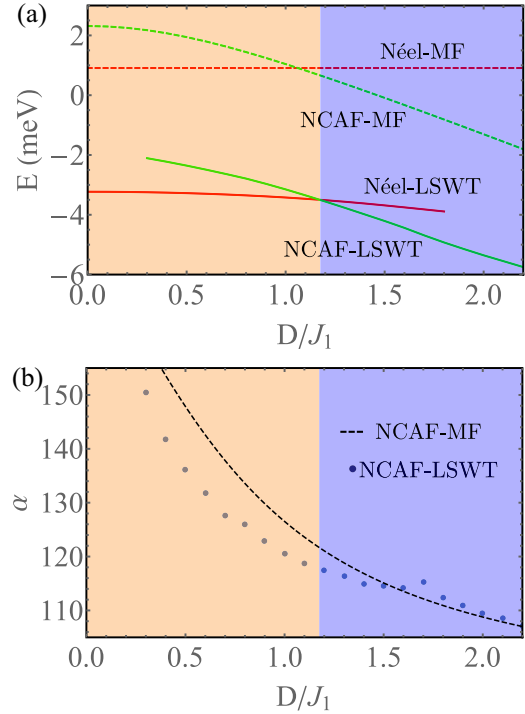

FIG. 9. (a) Energy of Néel and NCAF state as functions of DM strength D. Solid red (green) line corresponds to Néel (NCAF) states from LSWT. Dashed red (green) line corresponds to the MF energy of Néel (NCAF) states. (b) Angle α between T and O sites at different D. The dotted (dashed) line is from LSWT (MF). The orange region corresponds to Néel phase, where $\alpha = 180°$, whereas α is D dependent in the blue NCAF phase.

C. LSWT result

Since there is no coupling between the layers in our model (it is believed to be very small in $Ni_2Mo_3O_8$ [10]), our LSWT calculations are effectively two-dimensional. We note that the energy of the NCAF state depends on both angles α and θ_T. Under the fixed anisotropy parameters (see Sec. III) and exchange couplings determined from *ab initio* calculations (Sec. VI), we vary the strength of the DM interaction D and optimize the angles α and θ_T to obtain the minimum energy of the NCAF state.

The resulting phase diagram is shown in Fig. 9(a). The energy of the Néel (NCAF) state is represented by solid red (green) line, respectively. For comparison, the MF energies of these two states are represented by the dashed lines of the same colors. After we consider the zero-point fluctuation, the energies of both the Néel and NCAF states decrease compared with the MF result. The phase boundary between the two phases $D_c^{\text{LSW}} \approx 1.175J_1$ changes slightly from the MF result $D_c^{\text{MF}} \approx 1.06J_1$, which does not qualitatively affect any of our conclusions. In Fig. 9(b), we plot the optimal angle α between the spins on the T and O sites inside the NCAF phase as a function of DM interaction D, with the dotted (dashed) line corresponding to the LSWT (MF) results, respectively. Of course, the angle $\alpha = 180°$ for $D < D_c$ inside the Néel phase, so the plotted value of α is only meaningful on the right-hand side of the boundary where the NCAF phase becomes stable. Right at the phase boundary, the angle $\alpha \approx 115°$, and its value decreases almost monotonically with increasing D, except for
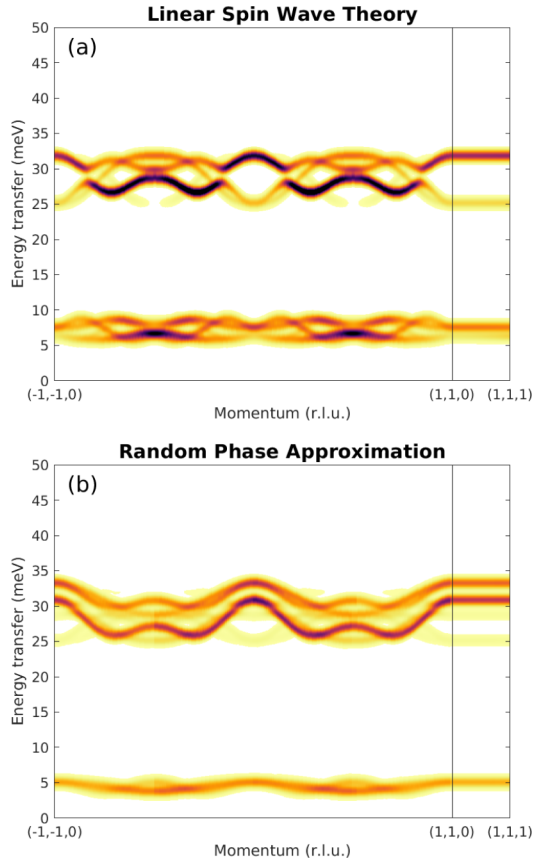
FIG. 10. Calculated magnetic excitation spectra using either (a) linear spin wave theory treating only the spin degree of freedom or (b) treating the full crystal field effects in a random phase approximation calculation.

an anomaly near $D/J_1 = 1.7$, which is due to the approximation of the biquadratic term as an anisotropic bilinear term as explained in the previous section.

In Fig. 10, we present the calculated excitation spectra using the spin-wave theory outlined above in a full lattice (with four T and four O sites per unit cell, which contains two honeycomb layers, which doubles the number of bands in our LSWT for a single layer). The upper panel (a) shows the calculated magnetic excitation spectrum with a spin-only LSWT using the SIA parameters γ_T and γ_O given in Sec. III and the DFT-derived exchange couplings from Eq. (13). The lower panel [Fig. 10(b)] shows the a calculation under the random phase approximation (RPA), which includes the full crystal field Hamiltonian. The color represents the neutron scattering intensities and an instrument resolution broadening of 1 meV was applied. In both cases, the DM interaction strength was fixed at $D = 3.1$ meV (just above $D_c = 1.175 J_1$). The SPINW [31] program was used for the calculations in Fig. 10(a) while MCPHASE [32] was used for those in Fig. 10(b).

Both calculations give two bands of excitations around 5 and 25 meV. The lower energy band is from the octahedral sites, while the higher energy excitations is associated with the tetrahedral sites, which have a larger SIA parameter γ_T in Eq. (6). The upper band dispersion is similar in the two calculations albeit the modes have different relative intensities, but the lower bands differ qualitatively. The differences arise due

to the way the two calculation methods treat the SIA, with the RPA theory being more accurate, as described in Appendix H.

IX. DISCUSSION

In this paper, we have proposed an effective spin model including the nearest-neighbor DM interaction to explain the noncollinear magnetic ordered state observed in a noncentrosymmetric honeycomb lattice material $Ni_2Mo_3O_8$ [10]. The reason for introducing the DM interaction is that it favors two neighboring spins to be perpendicular to each other, and competes with the bilinear $\vec{S}_i \cdot \vec{S}_j$ and biquadratic $(\vec{S}_i \cdot \vec{S}_j)^2$ terms, which usually favor two neighboring spins to be collinear [unless the biquadratic term is positive and large, see the discussion around Eq. (14), which is however not realized in $Ni_2Mo_3O_8$]. We show that without the DM interaction, the purely bilinear or bilinear-biquadratic model cannot reproduce the noncollinear magnetic order observed in $Ni_2Mo_3O_8$ [10].

We further argue that considering the *nearest-neighbor* DM interaction is sufficient. From Moriya's rules, the second-neighbor DM vector between two tetrahedral (T) or two octahedral (O) Ni spins lives in the plane which bisect the T–T (O–O) bond and is perpendicular to it. However, in both collinear states and NCAF states, the spins at next-nearest neighbor are collinear. As a result, the next-nearest-neighbor DM interaction does not affect their MF energies and gives only a small correction to the LSWT. It is furthermore difficult to imagine the spins in the same sublattice (T or O) to be noncollinear, given that the crystal-field environment and the magnetic anisotropy are the same on the two sites, corroborating the above conclusion that the next-nearest-neighbor DM interaction, even if present, does not contribute to the energies of the two competing states (Néel and NCAF). As for the third-neighbor and longer-range DM interactions, those are expected to be negligible, given the large separation between the magnetic moments.

In this paper, we also considered the effect of SIA, following the detailed crystal field analysis (see Sec. III). Although the crystal-field environments on T and O sites are different, it does not lead to noncollinear spin order. Moreover, because the crystal-field parameter $\gamma_T \gg \gamma_O$, the T spins prefer to lie close to the xy plane and in the absence of the DM interaction, remain collinear with the O spins.

In the experimental paper [10], several tentative scenarios were advanced to explain the noncollinear magnetic ordering in $Ni_2Mo_3O_8$. One of them was a bond-dependent Kitaev-like interaction, however, for it to be realized, the usual pathway is in systems with an edge-shared octahedral environment [33], which is not the case in $Ni_2Mo_3O_8$. Another possibility is that of a spiral state, which typically requires the exchange couplings J_1, J_2, J_3 up to third-nearest neighbors to all have similar magnitudes. This is, however, not the conclusion we have reached from our *ab initio* calculations, where we find J_3 ($\sim 10^{-2}$ meV) to be negligible. Finally, it was proposed [10] that bond-dependent anisotropic interactions, through ligand distortion, may be the cause of the noncollinear magnetic order to appear in $Ni_2Mo_3O_8$. While we cannot exclude this latter mechanism, we would argue that the DM interaction provides a more natural explanation and, as our results demon-

strate (see Figs. 4 and 7), the optimal value of angle α between neighboring spins is predicted to be close to the experimental value $\alpha' = 130°$ [10].

In summary, we have demonstrated that the NCAF ordered states in $Ni_2Mo_3O_8$ can be successfully understood as stemming from the first-neighbor DM interaction. Using a combination of first-principles electronic structure and product states' expected energy calculations, we have estimated the values of the exchange couplings, established the expected energy phase diagram, and found that a realistic value of DM interaction $D > D_c \approx 2.78$ meV is sufficient to stabilize the noncollinear magnetic order with the angle α_{opt} between the neighboring spins within a few degrees of the experimental value $\alpha' = 130°$.

We have performed the linear spin-wave calculations to include the fluctuations around the saddle-point solutions, and found that the inclusion of zero-point energies does not qualitatively affect the main conclusion, only shifting the critical value of DM interaction imperceptibly. We further make predictions for the magnon spectra inside the noncollinear magnetic phase, which should be compared to future inelastic neutron scattering data on $Ni_2Mo_3O_8$. Our calculations also indicate that when choosing between the two neutron scattering refinement fits reported in Ref. [10] and summarized in Table I, the first fit with the angle $\alpha' = 130°$ receives support from both the *ab initio* DFT results and our theoretical calculations.

The present paper opens an exciting avenue for investigating frustrated spin-1 systems with spin-orbit induced DM interactions. Application of the present ideas to different materials and lattices other than the honeycomb certainly deserve further attention.

ACKNOWLEDGMENTS

APPENDIX A: MEAN FIELD ENERGY OF VARIOUS STATES

The total Hamiltonian for spin $S = 1$ is

$$
\begin{aligned}
\mathcal{H}_{\text{eff}} = &\sum_{\langle ij \rangle} J_1 \vec{S}_i \cdot \vec{S}_j + K_1 (\vec{S}_i \cdot \vec{S}_j)^2 \\
&+ \sum_{\langle\langle ij \rangle\rangle, T} J_{2T} \vec{S}_i \cdot \vec{S}_j + K_{2T} (\vec{S}_i \cdot \vec{S}_j)^2 \\
&+ \sum_{\langle\langle ij \rangle\rangle, O} J_{2O} \vec{S}_i \cdot \vec{S}_j + K_{2O} (\vec{S}_i \cdot \vec{S}_j)^2 \\
&+ \sum_{\langle ij \rangle} \vec{D}_{ij} \cdot (\vec{S}_i \times \vec{S}_j) \\
&+ \sum_{i,T} \gamma_T (\vec{S}_i^z)^2 + \sum_{i,O} \gamma_O (\vec{S}_i^z)^2, \quad \text{(A1)}
\end{aligned}
$$

where the indices T and O denote the tetrahedral and octahedral Ni sites, respectively.

Based on the MF ansatz in Eqs. (9) and (10), we consider the interactions between two spins $\vec{S}_i$ and $\vec{S}_j$ parametrized by polar and azimuthal angles θ_i, ϕ_i, and θ_j, ϕ_j, respectively. The MF expressions of the terms in the Hamiltonian take the following form:

$$
\begin{aligned}
\langle \vec{S}_i \cdot \vec{S}_j \rangle &= \cos\alpha_{ij}, \\
\langle (\vec{S}_i \cdot \vec{S}_j)^2 \rangle &= \tfrac{1}{4}\cos^2\alpha_{ij} - \tfrac{1}{2}\cos\alpha_{ij} + \tfrac{1}{4} + 1, \\
\langle \vec{S}_i \times \vec{S}_j \rangle &= \sin\theta_i \sin\phi_i \cos\theta_j - \sin\theta_j \sin\phi_j \cos\theta_i \\
&\quad + \sin\theta_j \cos\phi_j \cos\theta_i - \sin\theta_i \cos\phi_i \cos\theta_j \\
&\quad + \sin\theta_i \cos\phi_i \sin\theta_j \sin\phi_j \\
&\quad - \sin\theta_i \sin\phi_i \sin\theta_j \cos\phi_j, \\
\langle (\vec{S}_i^z)^2 \rangle &= \tfrac{1}{2}\cos^2\theta_i + \tfrac{1}{2}, \quad \text{(A2)}
\end{aligned}
$$

where α_{ij} is the angle between two spin directions, $\cos\alpha_{ij} = \sin\theta_i \sin\theta_j \cos(\phi_i - \phi_j) + \cos\theta_i \cos\theta_j$. For simplicity, we get rid of a constant 1 in $\langle (\vec{S}_i \cdot \vec{S}_j)^2 \rangle$ term. With these MF results, we can obtain the average energy per site of the FM, Néel, stripe, zigzag, and NCAF state quoted in Eqs. (11) and (15):

$$
\begin{aligned}
\mathcal{E}^*_{\text{FM}} &= \tfrac{3}{2}J_1 + \tfrac{3}{2}J_{2T} + \tfrac{3}{2}J_{2O}, \\
\mathcal{E}^*_{\text{Néel}} &= -\tfrac{3}{2}J_1 + \tfrac{3}{2}K_1 + \tfrac{3}{2}J_{2T} + \tfrac{3}{2}J_{2O}, \\
\mathcal{E}^*_{\text{stripe}} &= -\tfrac{1}{2}J_1 + K_1 - \tfrac{1}{2}J_{2T} + K_{2T} - \tfrac{1}{2}J_{2T} + K_{2O}, \\
\mathcal{E}^*_{\text{zigzag}} &= \tfrac{1}{2}J_1 + \tfrac{1}{2}K_1 - \tfrac{1}{2}J_{2T} + K_{2T} - \tfrac{1}{2}J_{2T} + K_{2O}, \\
\mathcal{E}^*_{\text{NCAF}} &= \tfrac{1}{2}J_1 \cos\alpha + K_1 \left(\tfrac{3}{8}\cos^2\alpha - \tfrac{1}{4}\cos\alpha + \tfrac{3}{8} \right) \\
&\quad - \tfrac{1}{2}J_{2T} + K_{2T} - \tfrac{1}{2}J_{2O} + K_{2O} \\
&\quad - D(\sin\theta_O \cos\phi_O \cos\theta_T - \sin\theta_T \cos\phi_T \cos\theta_O),
\end{aligned}
$$
$$\text{(A3)}$$

where we use the asterisk (*) to label the energy without SIA. The contribution to the energy from the anisotropy term is

$$
\mathcal{E}_A(\theta_T, \theta_O) = \tfrac{1}{4}\gamma_T(\cos^2\theta_T + 1) + \tfrac{1}{4}\gamma_O(\cos^2\theta_O + 1). \quad \text{(A4)}
$$

We notice that the SIA is poorly captured by our *ab initio* DFT calculation, thus we can only solve six exchange parameters J_1, J_{2T}, J_{2O}, K_1, K_{2T}, and K_{2O}. The first four of the above equations are linearly dependent, and we therefore need at least three other noncollinear states to be able to solve for these six parameters. To make the result more accurate, we have increased the number of the reference states to 12 and perform least-squares fitting to obtain the exchange parameters. The other eight states are as follows.

First, we consider two collinear states which have FM order in T (O) sites and antiferromagnetic order in O (T) sites, as shown in Fig. 11(a). The energy expressions are

$$
\begin{aligned}
\mathcal{E}^*_1 &= \tfrac{3}{4}K_1 + \tfrac{3}{2}J_{2T} - \tfrac{1}{2}J_{2O} + K_{2O}, \\
\mathcal{E}^*_2 &= \tfrac{3}{4}K_1 + \tfrac{3}{2}J_{2O} - \tfrac{1}{2}J_{2T} + K_{2T}. \quad \text{(A5)}
\end{aligned}
$$

Then we rotate the spins at sublattice with FM order by 90°; there are two new collinear states:

$$
\begin{aligned}
\mathcal{E}^*_3 &= \tfrac{3}{8}K_1 + \tfrac{3}{2}J_{2T} - \tfrac{1}{2}J_{2O} + K_{2O}, \\
\mathcal{E}^*_4 &= \tfrac{3}{8}K_1 + \tfrac{3}{2}J_{2O} - \tfrac{1}{2}J_{2T} + K_{2T}. \quad \text{(A6)}
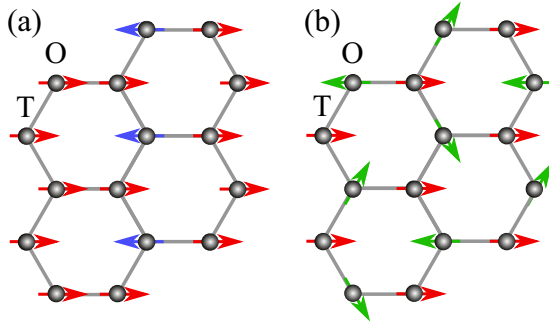\end{aligned}
$$

FIG. 11. The depiction of (a) a collinear state with ferromagnetic order in T sites and antiferromagnetic order in O sites and (b) a noncollinear state with ferromagnetic order in T sites and $120°$ antiferromagnetic order in O sites

Besides that, we introduce two noncollinear analogues of the Néel and zigzag states, obtained by rotating the spins on one of the sublattices (say, blue) in Figs. 2(d) and 2(f) respectively, such that the spins on the red and blue sublattices are perpendicular to each other. The MF energies of these two states are

$$\mathcal{E}_5^* = \tfrac{3}{8}K_1 + \tfrac{3}{2}J_{2T} + \tfrac{3}{2}J_{2O},$$
$$\mathcal{E}_6^* = J_1 + \tfrac{1}{8}K_1 + \tfrac{1}{2}J_{2T} + \tfrac{1}{4}K_{2T} + \tfrac{1}{2}J_{2O} + \tfrac{1}{4}K_{2O}. \quad \text{(A7)}$$

Finally, we consider two noncollinear states with FM order in T (O) sites and $120°$ antiferromagnetic order in O (T) sites, as shown in Fig. 11(b). The MF energies of these two states are

$$\mathcal{E}_7^* = \tfrac{3}{8}K_1 + \tfrac{3}{2}J_{2T} - \tfrac{3}{4}J_{2O} + \tfrac{27}{32}K_{2O},$$
$$\mathcal{E}_8^* = \tfrac{3}{8}K_1 + \tfrac{3}{2}J_{2O} - \tfrac{3}{4}J_{2T} + \tfrac{27}{32}K_{2T}. \quad \text{(A8)}$$

For all 12 states, we avoid the DM interaction, since DFT has difficulty accurately capturing those. With MF and DFT results of these reference states, we perform least-squares fitting to minimize the discrepancies between the analytical and *ab initio* energy differences of the references states:

$$\sum_i \left((\mathcal{E}_i^*(J, K) - \mathcal{E}_{\text{FM}}^*(J, K)) - (\mathcal{E}_i^{\text{DFT}} - \mathcal{E}_{\text{FM}}^{\text{DFT}}) \right)^2 \quad \text{(A9)}$$

under $|J_i| > |K_i|$, $J_{TF} - 2J_{TA} < 0$ and $J_{OF} - 2J_{OA} < 0$; the last two are weak constrains that stabilize the collinear antiferromagnetic ordered spins in two sublattices, J_{TF}, J_{TA}, J_{OF}, J_{OA} are effective Heisenberg exchange couplings introduced in Sec. VIII. This yields the values of the exchange parameters $J_1, K_1, J_{2T}, K_{2T}, J_{2O}$, and K_{2O} listed in Eq. (13) in the main text with a very good fit-quality factor $R^2 = 0.956$. The comparison between the *ab initio* and the resulting model energies is shown in Fig. 3 in the main text.

APPENDIX B: DETAILS OF *AB INITIO* ANALYSIS

We performed the first-principles DFT+U [34] calculations as implemented in the VASP package [35] using the projector augmented wave method [36], making use of generalized gradient approximations of Perdew-Burke-Ernzerhof (GGA-PBE) for exchange-correlation potential [37]. To extract the parameters of the effective spin model, we considered various possible magnetically ordered states, including FM, Néel, stripe, and zigzag, as well as the noncollinear NCAF
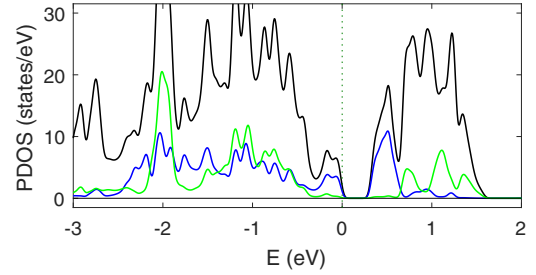

FIG. 12. The total electronic density of state (black line) in the Néel state of $Ni_2Mo_3O_8$. The partial contributions from Ni_T (green) and Ni_O (blue) electrons are also shown. The calculation was performed within DFT, with the Hubbard parameter $U = 0$. A clear band gap appears at the chemical potential, indicating that the magnetically ordered compound is a band insulator.

state. The base unit cell consisting of two stacked layers, with two Ni atoms per layer is sufficient to describe the the FM and Néel states. A $2 \times 1 \times 1$ supercell is used to describe the stripe and zigzag states, while a $2 \times 2 \times 1$ supercell is used to describe the NCAF state. We have performed the calculations without and with the Hubbard interaction $U = 3$ eV. The moments reported in Sec. VI in the main text were calculated for $U = 0$. On increasing the value of the Hubbard U to $U = 3$ eV, the total moments increased by about $0.2\mu_B$. The rest of our conclusions remain unchanged.

The density of states plots reveal the insulating nature of the compound, as shown in Fig. 12. There is an insulating gap even at Hubbard $U = 0$, which widens further with $U = 3$ eV. This suggests that $Ni_2Mo_3O_8$ is a Slater insulator, with the gap opening due to magnetism, rather than due to the Hubbard on-site repulsion.

APPENDIX C: CLASSICAL GROUND STATE WITHOUT SPIN-ORBIT COUPLING

In the main text, we consider the competition between two states—the Néel phase and the NCAF, see Fig. 4. This is justified *a posteriori* by comparing the energies of the two phases both at the MF level (Sec. V) and with zero-point fluctuations taken into account (Sec. VIII). Here, we provide an alternative, unbiased proof that the Néel antiferromagnet is indeed the classical ground state of the model in Eq. (1), before the DM interactions are taken into account.

We apply the classical Luttinger–Tisza method [38,39] to find the ground state of our model under the fitting parameters in Eq. (13), without DM interaction. We also ignore the SIA, since it lies beyond the classical approach described below.

First, we notice that the biquadratic spin interaction can be transformed into a quadrupolar interaction

$$(\vec{S}_i \cdot \vec{S}_j)^2 = \tfrac{1}{2}\vec{Q}_i \cdot \vec{Q}_j - \tfrac{1}{2}\vec{S}_i \cdot \vec{S}_j + \tfrac{1}{3}S^2(S+1)^2, \quad \text{(C1)}$$

where the five linearly independent quadrupolar components are

$$\begin{pmatrix} Q^{x^2-y^2} \\ Q^{3z^2-r^2} \\ Q^{xy} \\ Q^{yz} \\ Q^{zx} \end{pmatrix} = \begin{pmatrix} (S^x)^2 - (S^y)^2 \\ \frac{1}{\sqrt{3}}[3(S^z)^2 - S(S+1)] \\ S^x S^y - S^y S^x \\ S^y S^z - S^z S^y \\ S^z S^x - S^x S^z \end{pmatrix}. \quad \text{(C2)}$$

The quadrupolar and dipolar components are not independent and satisfy a strong constraint $(\vec{S}_i)^2 + (\vec{Q}_i)^2 = \frac{4}{3}$ on each site. In order to account for the possibility both dipolar and quadrupolar order, we introduce a constant $0 \leqslant \eta \leqslant 1$ (where $\eta = 1$ corresponds to a purely dipolar state), in terms of which we have two constraints:

$$\frac{1}{\beta_1^2}\sum_{i,T}(\vec{S}_i)^2 + \frac{1}{\beta_2^2}\sum_{i,O}(\vec{S}_i)^2 = \eta\frac{N}{2}\left(\frac{1}{\beta_1^2} + \frac{1}{\beta_2^2}\right),$$

$$\frac{1}{\beta_3^2}\sum_{i,T}(\vec{Q}_i)^2 + \frac{1}{\beta_4^2}\sum_{i,O}(\vec{Q}_i)^2 = \left(\frac{4}{3} - \eta\right)\frac{N}{2}\left(\frac{1}{\beta_3^2} + \frac{1}{\beta_4^2}\right)$$

(C3)

where β_1, β_3 (and β_2, β_4) are any real, nonzero numbers that capture the relative contribution of dipolar and quadrupolar moments on the T site (O site), respectively. Here N is the total number of sites. Introducing the Lagrange multipliers to enforce the above constraints on average, we obtain the following Lagrangian function, to be minimized:

$$\mathcal{L} = \sum_{\langle ij \rangle}\left(J_1 - \frac{K_1}{2}\right)\vec{S}_i \cdot \vec{S}_j + \frac{K_1}{2}(\vec{Q}_i \cdot \vec{Q}_j)^2 + \frac{4}{3}K_1$$

$$+ \sum_{\langle\langle ij \rangle\rangle,T}\left(J_{2T} - \frac{K_{2T}}{2}\right)\vec{S}_i \cdot \vec{S}_j + \frac{K_{2T}}{2}(\vec{Q}_i \cdot \vec{Q}_j)^2 + \frac{4}{3}K_{2T}$$

$$+ \sum_{\langle\langle ij \rangle\rangle,O}\left(J_{2O} - \frac{K_{2O}}{2}\right)\vec{S}_i \cdot \vec{S}_j + \frac{K_{2O}}{2}(\vec{Q}_i \cdot \vec{Q}_j)^2 + \frac{4}{3}K_{2O}$$

$$- \lambda^S\left(\frac{1}{\beta_1^2}\sum_{i,T}(\vec{S}_i)^2 + \frac{1}{\beta_2^2}\sum_{i,O}(\vec{S}_i)^2 - \eta\frac{N}{2}\left(\frac{1}{\beta_1^2} + \frac{1}{\beta_2^2}\right)\right)$$

$$- \lambda^Q\left(\frac{1}{\beta_3^2}\sum_{i,T}(\vec{Q}_i)^2 + \frac{1}{\beta_4^2}\sum_{i,O}(\vec{Q}_i)^2\right.$$

$$\left. - \left(\frac{4}{3} - \eta\right)\frac{N}{2}\left(\frac{1}{\beta_3^2} + \frac{1}{\beta_4^2}\right)\right).$$

(C4)

The minimum (more generally, saddle point) of this function satisfies the equations

$$\frac{\partial\mathcal{L}}{\partial\lambda^S} = 0, \quad \frac{\partial\mathcal{L}}{\partial\lambda^Q} = 0, \quad \frac{\partial\mathcal{L}}{\partial S_i^\alpha} = 0, \quad \frac{\partial\mathcal{L}}{\partial Q_i^\gamma} = 0, \quad (C5)$$

where the index $\alpha = x, y, z$ labels the spin components on a given site and $\gamma = x^2 - y^2, 3z^2 - r^2, xy, yz, zx$ labels the corresponding quadrupolar components. The first two equations enforce the two constraints in Eq. (C3). The other equations have the form of eigenvalue equations

$$\hat{M}_1(\vec{k})\begin{pmatrix} S_{T,\vec{k}}/\beta_1 \\ S_{O,\vec{k}}/\beta_2 \end{pmatrix} = 2\lambda_{\vec{k}}^S\begin{pmatrix} S_{T,\vec{k}}/\beta_1 \\ S_{O,\vec{k}}/\beta_2 \end{pmatrix},$$

$$\hat{M}_2(\vec{k})\begin{pmatrix} Q_{T,\vec{k}}/\beta_1 \\ Q_{O,\vec{k}}/\beta_2 \end{pmatrix} = 2\lambda_{\vec{k}}^Q\begin{pmatrix} Q_{T,\vec{k}}/\beta_1 \\ Q_{O,\vec{k}}/\beta_2 \end{pmatrix}, \quad (C6)$$

with matrices $\hat{M}_1$ and $\hat{M}_2$ defined as follows:

$$\hat{M}_1(\vec{k}) = \begin{pmatrix} \beta_1^2\left(J_{2T} - \frac{K_{2T}}{2}\right)g_{\vec{k}} & \beta_1\beta_2\left(J_1 - \frac{K_1}{2}\right)f_{\vec{k}} \\ \beta_1\beta_2\left(J_1 - \frac{K_1}{2}\right)f_{-\vec{k}} & \beta_2^2\left(J_{2O} - \frac{K_{2O}}{2}\right)g_{\vec{k}} \end{pmatrix},$$

$$\hat{M}_2(\vec{k}) = \begin{pmatrix} \beta_3^2\frac{K_{2T}}{2}g_{\vec{k}} & \beta_3\beta_4\frac{K_1}{2}f_{\vec{k}} \\ \beta_3\beta_4\frac{K_1}{2}f_{-\vec{k}} & \beta_4^2\frac{K_{2O}}{2}g_{\vec{k}} \end{pmatrix}, \quad (C7)$$

where

$$f_{\vec{k}} = e^{-i\left(\frac{1}{2}k_x + \frac{\sqrt{3}}{2}k_y\right)} + e^{ik_x} + e^{-i\left(\frac{1}{2}k_x - \frac{\sqrt{3}}{2}k_y\right)},$$

$$g_{\vec{k}} = 2\cos\left(\frac{3}{2}k_x - \frac{\sqrt{3}}{2}k_y\right) + 2\cos\sqrt{3}k_y$$

$$+ 2\cos\left(-\frac{3}{2}k_x - \frac{\sqrt{3}}{2}k_y\right).$$

In terms of the eigenvalues in Eq. (C6), the classical energy becomes

$$\epsilon(\vec{k}, \vec{k}') = \lambda_{\vec{k}}^S\eta\frac{N}{2}\left(\frac{1}{\beta_1^2} + \frac{1}{\beta_2^2}\right) + \lambda_{\vec{k}'}^Q\left(\frac{4}{3} - \eta\right)\frac{N}{2}\left(\frac{1}{\beta_3^2} + \frac{1}{\beta_4^2}\right)$$

$$+ \epsilon_0,$$

(C8)

where $\lambda_{\vec{k}}^S$, $\lambda_{\vec{k}'}^Q$ are the lowest eigenvalues of $\hat{M}_1(\vec{k})$, $\hat{M}_2(\vec{k})$ and ϵ_0 is a constant that only depends on the coupling constants.

The classical energy $E_{\text{class}} = \min_{k,k'}(\epsilon)$ is thus determined by minimizing $\lambda_{\vec{k}}^S(\frac{1}{\beta_1^2} + \frac{1}{\beta_2^2})$, $\lambda_{\vec{k}'}^Q(\frac{1}{\beta_3^2} + \frac{1}{\beta_4^2})$ with respect to the ordering wave vectors $\vec{k}$ and $\vec{k}'$ that parametrize the dipolar and quadrupolar spiral order, respectively. The next step is finding these wave vectors and the constants β_i that enter the constraints Eq. (C3). Without loss of generality, we can set $\beta_1 = \beta_3 = 1$, then β_2 and β_4 satisfy the relations $\beta_2 = |\psi_{S1}|/|\psi_{S2}|$ and $\beta_4 = |\psi_{Q1}|/|\psi_{Q2}|$, expressed in terms of the eigenvectors (ψ_{S1}, ψ_{S2}), (ψ_{Q1}, ψ_{Q2}) of Eq. (C6). After considering these two constrains, we finally obtain

$$\vec{k} = (0,0), \quad \vec{k}' = (0,0), \quad \beta_2 = 0.93, \quad \beta_4 = 1.39, \quad (C9)$$

signalling an intraunit cell order. Moreover, we find $\eta = 1$, which corresponds to a pure magnetic (dipolar) state. The two components of the eigenvector (ψ_{S1}, ψ_{S2}) have opposite sign on sites T and O, respectively, which means that the ground state has Néel order with the angle $\alpha = 180°$ between the two spins.

We note that while the Luttinger-Tisza method does not allow us to tackle the SIA explicitly, the effect of crystal fields in Eq. (6) with a large positive $\gamma_T \gg J_1 \gg |\gamma_O|$ is only to keep the Néel staggered moment in the xy plane. It is only once the effect of DM interactions is considered (Sec. V B) that a noncollinear order with the angle $\alpha \neq 180°$ between the T and O sites develops, as observed experimentally in $Ni_2Mo_3O_8$.

APPENDIX D: CLASSICAL GROUND STATE WITH SPIN-ORBIT COUPLING

In this Appendix, we find the ground state after including SOC—both the DM interaction and the SIA terms. Instead of the Luttinger–Tisza method, here we use classical spin configurations and minimize the classical energy, because the constraint of β_i in Appendix C becomes too complicated when spins on different sublattices and their components become nonequivalent.

We set the spins in each sublattice, forming a general coplanar spiral state, which is given by

$$\vec{S}_{T,i} = \mathbf{R}(\theta_T, \phi_T)\vec{S}'_{T,i}, \quad \vec{S}_{O,i} = \mathbf{R}(\theta_O, \phi_O)\vec{S}'_{O,i}, \quad (D1)$$

$$\mathbf{R}(\theta, \phi) = \begin{pmatrix} \cos\theta\cos\phi & -\sin\phi & \sin\theta\cos\phi \\ \cos\theta\sin\phi & \cos\phi & \sin\theta\sin\phi \\ -\sin\theta & 0 & \cos\theta \end{pmatrix}, \quad (D2)$$
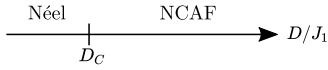
FIG. 13. The classical phase diagram as a function of the DM interaction strength D. The classical ground state is the Néel phase for small D. For larger $D > D_C = 1.18 J_1$, the ground state turns into the NCAF state.

where (θ_T, ϕ_T) and (θ_O, ϕ_O) determine the normal vectors of two planes spanned by spins on each sublattice, and the spin direction in local coordinates is written as $\vec{S}'_i = (\cos(\phi' + \vec{k} \cdot \vec{r}_i), \sin(\phi' + \vec{k} \cdot \vec{r}_i), 0)^T$, with i labeling the unit cell and $\vec{k}$ the magnetic wave vector. Explicitly, the spin configurations are

$$S^x_{T,i} = \cos\theta_T \cos\phi_T \cos(\phi'_T + \vec{k} \cdot \vec{r}_i) - \sin\phi_T \sin(\phi'_T + \vec{k} \cdot \vec{r}_i),$$

$$S^y_{T,i} = \cos\theta_T \sin\phi_T \cos(\phi'_T + \vec{k} \cdot \vec{r}_i) + \cos\phi_T \sin(\phi'_T + \vec{k} \cdot \vec{r}_i),$$

$$S^z_{T,i} = -\sin\theta_T \cos(\phi'_T + \vec{k} \cdot \vec{r}_i)$$

$$S^x_{O,i} = \cos\theta_O \cos\phi_O \cos(\phi'_O + \vec{k} \cdot \vec{r}_i) - \sin\phi_O \sin(\phi'_O + \vec{k} \cdot \vec{r}_i),$$

$$S^y_{O,i} = \cos\theta_O \sin\phi_O \cos(\phi'_O + \vec{k} \cdot \vec{r}_i) + \cos\phi_T \sin(\phi'_O + \vec{k} \cdot \vec{r}_i),$$

$$S^z_{O,i} = -\sin\theta_O \cos(\phi'_O + \vec{k} \cdot \vec{r}_i). \tag{D3}$$

We bring Eq. (D3) into Eq. (A1) to obtain the classical energy, then minimize it to find the magnetic wave vector of the ground state.

The classical phase diagram is shown in Fig. 13. We find that the ground state is a coplanar spin state with spins staying in xz plane. If the DM strength is sufficiently weak $D < D_C \approx 1.18 J_1$, we find the magnetic wave vector $\vec{k} = (0, 0)$, i.e., the intra-unit-cell order with antialigned spins, which means that the ground state is Néel ordered. For larger DM interaction strength $D > D_C$, the ground state becomes the NCAF state with $\vec{k} = (2\pi/3, 0)$.

APPENDIX E: CRYSTAL FIELD ANALYSIS: POINT-CHARGE MODEL

As discussed by Morey *et al.* [10], the crystal field plays an important role in Ni$_2$Mo$_3$O$_8$. The previous work used a simple point-charge model to determine the crystal field splitting. This model included only the coordinating oxygen ions around each Ni^{2+} ion and used the nominal charge for the neighbor ligands (i.e., $-2|e|$ for O^{2-}). The work also showed that without SOC, the two lowest-lying crystal-field levels are an orbital singlet ^3A ground state and an orbital doublet ^3E excited state. Repeating the calculation, we found that the ^3E level for the octahedral site is at around 330 meV and does not affect the ground state. The *tetrahedral* site, however, has its ^3E level at a much lower energy, around 48 meV, which is of the same order of magnitude as the SOC ($\lambda \approx 40$ meV). Thus, one should expect the SOC to mix these two orbital levels, leading to a large splitting of the orbital singlet (but spin triplet) ^3A, which is indeed what Morey *et al.* [10] found, with a splitting of ≈ 23 meV between the Γ_1 spin-singlet ground state and Γ_3 spin-doublet excited state.

The small splitting of the ^3E level also implies that there should be crystal field excitations above this 23 meV level but below 100 meV visible in the neutron spectra (the full

calculation implies excitations around 80 meV). However, recent extensive inelastic neutron scattering experiments [40] showed no evidence of this.

Furthermore, the spin-singlet Γ_1 ground state implies an effective planar SIA with it being highly favorable energetically for the spins to lie in the ab plane. The experimentally determined magnetic structures, however, suggest that the spin on one site is canted by a relatively large angle away from the ab plane. In the case of model 1 (2), this is the octahedral (tetrahedral) site at an angle of $\theta_O - \frac{\pi}{2} = 55°$ ($\theta_T - \frac{\pi}{2} = 34°$). Note that the polar angles θ_T and θ_O in Table I are relative to the c axis.

These experimental findings suggests that the point-charge model of Morey *et al.* [10] needs some adjustments. In particular, we believe that (1) the splitting between the ^3E and ^3A orbital levels on the tetrahedral site should be much larger and that (2) the ground state on one of the sites should be the doublet Γ_3 or a quasitriplet rather than the spin-singlet Γ_1. We can modify the point-charge model to satisfy condition 1 by increasing the effective magnitude of the point charges (which increases the magnitude of the crystal field parameters and thus increases the splitting). Condition 2 can be satisfied by including the effects of the Mo^{4+} and Ni^{2+} ions in addition to the O^{2-} in the model, and then either increasing the relative magnitude of the effective charge of the Mo^{4+} ions or decreasing that of the Ni^{2+} ions (even to making it negative) with respect to that of the O^{2-} ions.

We opted to do both, and posit a point-charge model with effective charges which are approximately twice the nominal charges: an effective charge of $-4|e|$ on the oxygen ligands, $+9|e|$ on the molybdenum ligands, and $+1|e|$ on the nickel ligands. The model includes ligands up to 3.5 Å away from the magnetic nickel ions, which covers to the nearest molybdenum ligands for each site. This model yields the crystal field parameters shown in Eq. (4) in the main text.

This model yields the ^3A–^3E splitting of 95 meV on the tetrahedral sites and much larger, 950 meV on octahedral sites. The tetrahedral sites still have a Γ_1 spin-singlet ground state, with the Γ_3 excited state at ≈ 24 meV and a further excitation at ≈ 125 meV, which may be visible in inelastic neutron scattering data. This structure of the $\Gamma_1 - \Gamma_3$ splitting is captured by the relatively large positive value $\gamma_T \approx 30$ meV in the effective spin anisotropy model Eq. (6). The octahedral site, on the other hand, has a Γ_3 spin-doublet ground state with a very low-lying Γ_1 excited state at ≈ 0.5 meV. In the effective spin anisotropy model Eq. (6), this is reflected in the very small (negative) value of $\gamma_O \approx -0.5$ meV.

Physically, larger magnitudes of the effective charges imply that Ni$_2$Mo$_3$O$_8$ has strong covalent bonds or large charge-transfer energies. The larger relative effective charge on the Mo^{4+} ions compared to that on the O^{2-} perhaps reflects the larger extent of the $4d$ orbitals which thus effectively reduces the distance between the magnetic nickel ions and the molybdenum ligand, while the smaller relative effective charge on neighboring Ni^{2+} ions reflects a more itinerant character of the nickel conduction electrons.

Finally, the large difference in the Γ_1-Γ_3 splittings for the different sites (octahedral and tetrahedral) in both the original [10] and our point-charge models means that the magnetic excitation spectrum comprises separate bands for the different

sites: a low energy magnonlike set of excitations from the octahedral sites and a higher energy excitonlike set of excitations from the tetrahedral sites. This is indeed seen in the computed magnetic excitation spectra in Fig. 10.

APPENDIX F: CRYSTAL FIELD ANALYSIS: SINGLE ION ANISOTROPY PARAMETERS

Due to the threefold rotation symmetry C_3 in the $P6_3mc$ space group, the crystal-field Hamiltonian is given by Eq. (3) in the main text:

$$\mathcal{H}_{\text{cf}} = L_{20}\theta_2\hat{T}_{20} + L_{40}\theta_4\hat{T}_{40} + L_{43}\theta_4\hat{T}_{43}. \qquad \text{(F1)}$$

Here L_{lm} are the crystal-field parameters whose values in Eq. (4) were derived from the point-charge model, the coefficients θ_l are the Stevens factors from MCPHASE [32] calculation,

$$\theta_2 = 0.0190, \quad \theta_4 = 0.0063, \qquad \text{(F2)}$$

and $\hat{T}_{lm}$ are tensorial Stevens–Wybourne operators,

$$\hat{T}_{20} = \frac{1}{2}\big(3\hat{L}_z^2 - X\big),$$

$$\hat{T}_{40} = \frac{1}{8}\big(35\hat{L}_z^4 - (30X - 25)\hat{L}_z^2 + 3X^2 - 6X\big),$$

$$\hat{T}_{43} = \frac{\sqrt{35}}{8}((\hat{L}_+^3 + \hat{L}_-^3)\hat{L}_z + \hat{L}_z(\hat{L}_+^3 + \hat{L}_-^3)), \qquad \text{(F3)}$$

where $\hat{L}_+$, $\hat{L}_-$ are the ladder operators of the orbital angular momentum and $\hat{L}_z$ is its z component. Here $X = l(l + 1)$, which in the present case of Ni^{2+} ($3d^8$) ion with $l = 3$ gives $X = 12$.

Substituting one set of crystal-field parameters and the matrix form of operators $\hat{L}_+$, $\hat{L}_-$, and $\hat{L}_z$, the crystal-field Hamiltonian becomes a 7×7 matrix, and we denote its eigenstates and corresponding eigenvalues $|n\rangle$ and E_n, respectively, with the ground state labeled by $n = 0$. Because the value of the coupling constant $\lambda \approx -40$ meV (see Ref. [24]) is much smaller than the difference of crystal field energy eigenvalues, the SOC $V = \lambda\vec{S} \cdot \vec{L}$ can be treated as a perturbation. The first order of the perturbation is proportional to $\langle 0|\vec{S} \cdot \vec{L}|0\rangle$, which vanishes identically. The correction to the energy in the second-order perturbation theory is of the form

$$E_0^{\text{2nd}} = \sum_{m>0}\frac{|\langle 0|V|m\rangle|^2}{E_0 - E_m} = \lambda^2\sum_{ij}\Lambda_{ij}S^iS^j, \qquad \text{(F4)}$$

where

$$\Lambda_{ij} = \sum_{m>0}\frac{\langle 0|L_i|m\rangle\langle m|L_j|0\rangle}{E_0 - E_m} \qquad \text{(F5)}$$

is the SIA parameter. Finally, we obtain the effective single-ion spin anisotropy Hamiltonian in Eq. (6) of the main text,

$$\mathcal{H}_A = \sum_T\gamma_T\big(S_i^z\big)^2 + \sum_O\gamma_O\big(S_i^z\big)^2, \qquad \text{(F6)}$$

with numerical values of the coefficients $\gamma_T = 30.41$ meV, $\gamma_O = -0.53$ meV.

We also investigate the contribution of higher-order perturbation theory to the values of single-ion anisotropy parameters

in Eq. (F6). The third order of the perturbation theory vanishes. The correction to the energy in the fourth order perturbation theory is of the form:

$$E_0^{4th} = \sum_{m>0}\sum_{n>0}\sum_{p>0}\frac{\langle 0|V|m\rangle\langle m|V|n\rangle\langle n|V|p\rangle\langle p|V|0\rangle}{(E_0 - E_m)(E_0 - E_n)(E_0 - E_p)}$$

$$- E_0^{2nd}\sum_{m>0}\frac{|\langle 0|V|m\rangle|^2}{(E_0 - E_m)^2}$$

$$= \lambda^4\sum_{ijkl}\Lambda_{ijkl}S^iS^jS^kS^l. \qquad \text{(F7)}$$

As an estimate of the effect that this fourth order term has onto the single-ion anisotropy, we calculate the diagonal terms. On tetrahedral site it gives

$$\Delta H_T^{(4)} = 10.64\big(S_T^x\big)^4 + 10.64\big(S_T^y\big)^4 + 0.09\big(S_T^z\big)^4, \qquad \text{(F8)}$$

which lowers the crystal field energy splitting (our estimate is the effective renormalization of γ_T down to ≈ 17 meV in Eq. (F6)). On the octahedral site, we similarly find the additional contribution

$$\Delta H_O^{(4)} = 0.019\big(S_O^x\big)^4 + 0.019\big(S_O^y\big)^4 + 0.018\big(S_O^z\big)^4, \qquad \text{(F9)}$$

which only provides a small correction (of the order of 0.002 meV) to $\gamma_O = -0.53$ meV. We note that while this value is negative, i.e. favors a doublet on the octahedral site, it should be noted that a small positive value of γ_O, favouring the $S^z = 0$ singlet, fits the inelastic neutron scattering (INS) data equally well.

APPENDIX G: LSWT CALCULATION

The full Hamiltonian of the effective Heisenberg model for the Néel state consists of the exchange interactions in Eq. (24), with the addition of the DM interaction and the SIA:

$$\mathcal{H}_{\text{Néel}}^{\text{e}} = \sum_{\langle ij\rangle}J_1^{\text{e}}\vec{S}_i \cdot \vec{S}_j + \sum_{\langle ij\rangle}\vec{D}_{ij} \cdot (\vec{S}_i \times \vec{S}_j)$$

$$+ \sum_{\langle\langle ij\rangle\rangle,T}J_{2T}^{\text{e}}\vec{S}_i \cdot \vec{S}_j + \sum_{\langle\langle ij\rangle\rangle,O}J_{2O}^{\text{e}}\vec{S}_i \cdot \vec{S}_j$$

$$+ \sum_{i,T}\gamma_T\big(S_i^z\big)^2 + \sum_{i,O}\gamma_O\big(S_i^z\big)^2. \qquad \text{(G1)}$$

The effective coupling constants J_1^{e}, J_{2T}^{e}, and J_{2O}^{e} are quoted in Eq. (25) in the main text. After the HP transformation in Eq. (28), the Hamiltonian becomes

$$\mathcal{H}_{\text{Néel}}^{\text{e}} = \mathcal{E}_{\text{Néel}} + \mathcal{E}_C + \sum_{\vec{k}}\psi_{\vec{k}}^\dagger H(\vec{k})\psi_{\vec{k}}, \qquad \text{(G2)}$$

where $\mathcal{E}_{\text{Néel}}$ is the MF energy expression, $\mathcal{E}_C$ is a constant term originating from the commutation relation when we construct the bosonic Nambu representation. Here the composite vector $\psi_{\vec{k}} = [a(\vec{k}), b(\vec{k}), a^\dagger(-\vec{k}), b^\dagger(-\vec{k})]^{\mathsf{T}}$ consists of the bosonic operators a on the T site and operators b on O sites. The matrix

$H(\vec{k})$ is

$$
H(\vec{k}) = \begin{pmatrix} f_T(\vec{k}) & 0 & \frac{\gamma_T}{2} & g(\vec{k}) \\ 0 & f_O(\vec{k}) & g(-\vec{k}) & \frac{\gamma_O}{2} \\ \frac{\gamma_T}{2} & g(-\vec{k})^* & f_T(\vec{k}) & 0 \\ g(\vec{k})^* & \frac{\gamma_O}{2} & 0 & f_O(-\vec{k}) \end{pmatrix}, \quad (G3)
$$

where

$$
\begin{aligned}
f_T(\vec{k}) = {} & \frac{3}{2}J_1^e - 3J_{2T}^e + \frac{1}{2}\gamma_T + J_{2T}^e\left(\cos\left(\frac{3}{2}k_x - \frac{\sqrt{3}}{2}k_y\right)\right. \\
& \left. + \cos\sqrt{3}k_y + \cos\left(-\frac{3}{2}k_x - \frac{\sqrt{3}}{2}k_y\right)\right),
\end{aligned}
$$

$$
\begin{aligned}
f_O(\vec{k}) = {} & \frac{3}{2}J_1^e - 3J_{2O}^e + \frac{1}{2}\gamma_O + J_{2O}^e\left(\cos\left(\frac{3}{2}k_x - \frac{\sqrt{3}}{2}k_y\right)\right. \\
& \left. + \cos\sqrt{3}k_y + \cos\left(-\frac{3}{2}k_x - \frac{\sqrt{3}}{2}k_y\right)\right),
\end{aligned}
$$

$$
\begin{aligned}
g(\vec{k}) = {} & -\frac{1}{2}J_1^e(e^{-i(\frac{1}{2}k_x + \frac{\sqrt{3}}{2}k_y)} + e^{ik_x} + e^{-i(\frac{1}{2}k_x - \frac{\sqrt{3}}{2}k_y)}) \\
& -iD\left(e^{-i(\frac{1}{2}k_x + \frac{\sqrt{3}}{2}k_y)}\sin\left(\phi + \frac{2\pi}{3}\right) + e^{ik_x}\sin\phi\right. \\
& \left. + e^{-i(\frac{1}{2}k_x - \frac{\sqrt{3}}{2}k_y)}\sin\left(\phi + \frac{4\pi}{3}\right)\right). \quad (G4)
\end{aligned}
$$

Above, ϕ is the azimuthal angle of the spin direction in xy plane. The constant $\mathcal{E}_C$ in Eq. (G3) is given by

$$
\mathcal{E}_C = -\frac{3\sqrt{3}}{4(2\pi)^2}\int_{BZ} d^2k(f_T(\vec{k}) + f_O(\vec{k})). \quad (G5)
$$

After the Bogoliubov transformation, the LSWT energy of Néel state becomes

$$
\mathcal{E}_{\text{Néel}}^{\text{LSWT}} = \mathcal{E}_{\text{Néel}} + \mathcal{E}_C + \frac{3\sqrt{3}}{4(2\pi)^2}\int_{1\text{BZ}}(E_a(\vec{k}) + E_b(\vec{k})), \quad (G6)
$$

where $E_a(\vec{k})$ and $E_b(\vec{k})$ are the two positive eigenvalues of the matrix Eq. (G3), corresponding physically to the two bands in the magnetic spectrum. Having fixed the exchange couplings to their *ab initio* values in Eq. (13) and the SIA parameters as quoted below Eq. (6), our calculations show that the Néel state has the minimum energy for the azimuthal angle $\phi = 30°$.

The full Hamiltonian of the effective Heisenberg model for the NCAF state is given by the spin bilinear in Eqs. (26) and (27) in the main text, with the addition of the DM interaction and single-ion spin anisotropy terms, analogous to Eq. (G1) above.

After the HP transformation in Eq. (28), the Hamiltonian becomes

$$
\mathcal{H} = \mathcal{E}_{\text{NCAF}} + \mathcal{E}_C + H_{\text{lin}}[b^\dagger, b] + \psi_{\vec{k}}^\dagger H(\vec{k})\psi_{\vec{k}}, \quad (G7)
$$

where $\mathcal{E}_{\text{NCAF}}$ is the MF energy and $H_{\text{lin}}[b^\dagger, b]$ collects the terms linear in the boson creation and annihilation operators (these terms are ignored in what follows as they do not conserve the magnon number).

The composite vector $\psi_{\vec{k}}$ of creation-annihilation operators is given by

$$
\begin{aligned}
\psi = {} & [a(\vec{k}), a^\dagger(-\vec{k}), b(\vec{k}), b^\dagger(-\vec{k}), c(\vec{k}), \\
& c^\dagger(-\vec{k}), d(\vec{k}), d^\dagger(-\vec{k})]^\mathsf{T}, \quad (G8)
\end{aligned}
$$

where a and c are annihilation operators at aT and $-T$ sites, whereas b and d annihilate bosons on the O and $-O$ sites [see Fig. 8(b) for the notation of the sites]. The matrix $H(\vec{k})$ in Eq. (G7) is given by

$$
H(\vec{k}, \vec{\theta}) = \frac{1}{2}\begin{pmatrix} H_{11}(\vec{k}, \vec{\theta}) & H_{12}(\vec{k}, \vec{\theta}) \\ H_{12}^\dagger(\vec{k}, \vec{\theta}) & H_{11}^\mathsf{T}(-\vec{k}, \vec{\theta}) \end{pmatrix}, \quad (G9)
$$

with the entries

$$
H_{11}(\vec{k}) = \begin{pmatrix} f_a(\vec{k}, \vec{\theta}) & 0 & f_{ab}(\vec{k}, \vec{\theta}) & f_{ad}(\vec{k}, \vec{\theta}) \\ 0 & f_c(\vec{k}, \vec{\theta}) & f_{cb}(\vec{k}, \vec{\theta}) & f_{cd}(\vec{k}, \vec{\theta}) \\ f_{ab}^*(\vec{k}, \vec{\theta}) & f_{cb}^*(\vec{k}, \vec{\theta}) & f_b(\vec{k}, \vec{\theta}) & 0 \\ f_{ad}^*(\vec{k}, \vec{\theta}) & f_{cd}^*(\vec{k}, \vec{\theta}) & 0 & f_d(\vec{k}, \vec{\theta}) \end{pmatrix},
$$

$$
H_{12}(\vec{k}) = \begin{pmatrix} g_a(\vec{k}, \vec{\theta}) & g_{ac}(\vec{k}, \vec{\theta}) & g_{ab}(\vec{k}, \vec{\theta}) & g_{ad}(\vec{k}, \vec{\theta}) \\ g_{ac}(-\vec{k}, \vec{\theta}) & g_c(\vec{k}, \vec{\theta}) & g_{cb}(\vec{k}, \vec{\theta}) & g_{cd}(\vec{k}, \vec{\theta}) \\ g_{ab}(-\vec{k}, \vec{\theta}) & g_{cb}(-\vec{k}, \vec{\theta}) & g_b(-\vec{k}, \vec{\theta}) & g_{bd}(\vec{k}, \vec{\theta}) \\ g_{ad}(-\vec{k}, \vec{\theta}) & g_{cd}(-\vec{k}, \vec{\theta}) & g_{bd}(-\vec{k}, \vec{\theta}) & g_d(\vec{k}, \vec{\theta}) \end{pmatrix},
$$

where $\vec{\theta} = (\theta_O, \theta_T)$, and the matrix elements are given by a lengthy set of expressions shown here for completeness:

$$
\begin{aligned}
f_a(\vec{k}, \theta_T, \theta_O) = {} & -2J_{1+}\cos(\theta_T + \theta_O) + J_{1-}\cos(\theta_T + \theta_O) \\
& -2J_{TF} + 4J_{TA} \\
& +2J_{TF}\cos\sqrt{3}k_y + 2D\sin(\theta_T + \theta_O) \\
& +\gamma_T(\sin^2\theta_T - 2\cos^2\theta_T),
\end{aligned}
$$

$$
\begin{aligned}
f_b(\vec{k}, \theta_T, \theta_O) = {} & -2J_{1+}\cos(\theta_T + \theta_O) + J_{1-}\cos(\theta_T + \theta_O) \\
& -2J_{OF} + 4J_{OA} \\
& +2J_{OF}\cos\sqrt{3}k_y + 2D\sin(\theta_T + \theta_O) \\
& +\gamma_O(\sin^2\theta_T - 2\cos^2\theta_T),
\end{aligned}
$$

$$
\begin{aligned}
f_c(\vec{k}, \theta_T, \theta_O) = {} & f_a(\vec{k}, \theta_T, \theta_O), \\
f_d(\vec{k}, \theta_T, \theta_O) = {} & f_b(\vec{k}, \theta_T, \theta_O), \quad (G10)
\end{aligned}
$$

$$
\begin{aligned}
f_{ab}(\vec{k}, \theta_T, \theta_O) = {} & \left(\frac{J_{1+}(\vec{\theta})}{2}(\cos(\theta_T + \theta_O) + 1)\right. \\
& -\frac{D}{4}\sin(\theta_T + \theta_O) \\
& \left. +\frac{\sqrt{3}}{4i}D(\sin\theta_O - \sin\theta_T)\right)e^{-i(\frac{1}{2}k_x + \frac{\sqrt{3}}{2}k_y)} \\
& +\left(\frac{J_{1+}(\vec{\theta})}{2}(\cos(\theta_T + \theta_O) + 1)\right. \\
& -\frac{D}{4}\sin(\theta_T + \theta_O) \\
& \left. -\frac{\sqrt{3}}{4i}D(\sin\theta_O - \sin\theta_T)\right)e^{-i(\frac{1}{2}k_x - \frac{\sqrt{3}}{2}k_y)},
\end{aligned}
$$

$$f_{ad}(\vec{k}, \theta_T, \theta_O) = \left(\frac{J_{1-}(\vec{\theta})}{2}(1 - \cos(\theta_T + \theta_O)) \right.$$
$$\left. - \frac{D}{2}\sin(\theta_T + \theta_O) \right) e^{ik_x},$$

$$f_{cb}(\vec{k}, \theta_T, \theta_O) = f_{ad}(\vec{k}, \theta_T + \pi, \theta_O + \pi),$$
$$f_{cd}(\vec{k}, \theta_T, \theta_O) = f_{ab}(\vec{k}, \theta_T + \pi, \theta_O + \pi), \qquad (G11)$$

$$g_a(\vec{k}, \theta_T, \theta_O) = g_c(\vec{k}, \theta_T, \theta_O) = \gamma_T \sin^2\theta_T,$$
$$g_b(\vec{k}, \theta_T, \theta_O) = g_d(\vec{k}, \theta_T, \theta_O) = \gamma_O \sin^2\theta_O,$$
$$g_{ac}(\vec{k}, \theta_T, \theta_O) = -4J_{TA}\cos\frac{3k_x}{2}\cos\frac{\sqrt{3}k_y}{2}$$
$$g_{bd}(\vec{k}, \theta_T, \theta_O) = -4J_{OA}\cos\frac{3k_x}{2}\cos\frac{\sqrt{3}k_y}{2}$$

$$g_{ab}(\vec{k}, \theta_T, \theta_O) = \left(\frac{J_{1+}(\vec{\theta})}{2}(\cos(\theta_T + \theta_O) - 1) \right.$$
$$- \frac{D}{4}\sin(\theta_T + \theta_O)$$
$$\left. + \frac{\sqrt{3}}{4i}D(\sin\theta_O + \sin\theta_T) \right) e^{-i(\frac{1}{2}k_x + \frac{\sqrt{3}}{2}k_y)}$$
$$+ \left(\frac{J_{1+}(\vec{\theta})}{2}(\cos(\theta_T + \theta_O) - 1) \right.$$
$$- \frac{D}{4}\sin(\theta_T + \theta_O)$$
$$\left. - \frac{\sqrt{3}}{4i}D(\sin\theta_O + \sin\theta_T) \right) e^{-i(\frac{1}{2}k_x - \frac{\sqrt{3}}{2}k_y)},$$

$$g_{ad}(\vec{k}, \theta_T, \theta_O) = \left(-\frac{J_{1-}(\vec{\theta})}{2}(1 + \cos(\theta_T + \theta_O)) \right.$$
$$\left. - \frac{D}{2}\sin(\theta_T + \theta_O) \right) e^{ik_x},$$

$$g_{cb}(\vec{k}, \theta_T, \theta_O) = g_{ad}(\vec{k}, \theta_T + \pi, \theta_O + \pi),$$
$$g_{cd}(\vec{k}, \theta_T, \theta_O) = g_{ab}(\vec{k}, \theta_T + \pi, \theta_O + \pi). \qquad (G12)$$

This results in the constant contribution to the energy $\mathcal{E}_C$:

$$\mathcal{E}_C = -\frac{3\sqrt{3}}{4(2\pi)^2}\int_{BZ} d^2k (f_a(\vec{k}) + f_b(\vec{k}) + f_c(\vec{k}) + f_d(\vec{k})). \qquad (G13)$$

After the Bogoliubov transformation, the energy of the NCAF state within LSWT is finally given by

$$\mathcal{E}_{NCAF}^{LSWT} = \mathcal{E}_{NCAF} + \mathcal{E}_C + \frac{3\sqrt{3}}{4(2\pi)^2}\int_{1BZ}(E_a(\vec{k})$$
$$+ E_b(\vec{k}) + E_c(\vec{k}) + E_d(\vec{k})). \qquad (G14)$$

The resulting energy of the NCAF state is computed by summing over the real, positive eigenvalues of the matrix $H(\vec{k}, \theta_T, \alpha)$ in Eq. (G9) and optimizing the angles α and θ_T such as to minimize this energy. The resulting optimal values of α are shown in Fig. 9 in the main text as a function of the varying DM interaction strength.

APPENDIX H: MAGNETIC EXCITATION SPECTRUM

In LSWT, the SIA is a constant term added to the diagonal of the Hamiltonian matrix. The resulting magnetic spectrum is shown in Fig. 10(a) in the main text. On the other hand, in the RPA calculations the full single-ion Hamiltonian matrix is calculated first and diagonalized, then an RPA coupling is made for each dipolar transition between the single-ion states. Given the large difference in the SIA between the tetrahedral (large gap) and octahedral (small gap) sites, the result is that in the RPA calculation, despite the large nearest-neighbor J_1 and K_1 interactions there is little coupling between the modes associated with the tetrahedral and octahedral sites. In contrast, in LSWT the additional diagonal constants in the Hamiltonian serve to separate out the tetrahedral and octahedral modes in energy but the off-diagonal terms in the Hamiltonian still results in significant coupling between the sites, which thus modifies the dispersion. One can see the resulting differences by comparing the magnetic spectra in the two panels in Fig. 10. Given the relatively large SIA, we believe that its treatment in LSWT is less accurate than with the RPA, but this should be confirmed by experimental measurements of the magnetic excitation spectrum.

[1] A. Kitaev, Ann. Phys. **321**, 2 (2006).

[2] G. Jackeli and G. Khaliullin, Phys. Rev. Lett. **102**, 017205 (2009).

[3] Y. Singh and P. Gegenwart, Phys. Rev. B **82**, 064412 (2010).

[4] Y. Singh, S. Manni, J. Reuther, T. Berlijn, R. Thomale, W. Ku, S. Trebst, and P. Gegenwart, Phys. Rev. Lett. **108**, 127203 (2012).

[5] K. W. Plumb, J. P. Clancy, L. J. Sandilands, V. V. Shankar, Y. F. Hu, K. S. Burch, H.-Y. Kee, and Y.-J. Kim, Phys. Rev. B **90**, 041112(R) (2014).

[6] K. Kitagawa, T. Takayama, Y. Matsumoto, A. Kato, R. Takano, Y. Kishimoto, S. Bette, R. Dinnebier, G. Jackeli, and H. Takagi, Nature (London) **554**, 341 (2018).

[7] F. D. M. Haldane, Phys. Rev. Lett. **50**, 1153 (1983).

[8] I. Affleck, J. Phys.: Condens. Matter **1**, 3047 (1989).

[9] J. R. Chamorro, L. Ge, J. Flynn, M. A. Subramanian, M. Mourigal, and T. M. McQueen, Phys. Rev. Mater. **2**, 034404 (2018).

[10] J. R. Morey, A. Scheie, J. P. Sheckelton, C. M. Brown, and T. M. McQueen, Phys. Rev. Mater. **3**, 014410 (2019).

[11] E. A. Zvereva, M. I. Stratan, Y. A. Ovchenkov, V. B. Nalbandyan, J.-Y. Lin, E. L. Vavilova, M. F. Iakovleva, M. Abdel-Hafiez, A. V. Silhanek, X.-J. Chen, A. Stroppa, S. Picozzi, H. O. Jeschke, R. Valentí, and A. N. Vasiliev, Phys. Rev. B **92**, 144401 (2015).

[12] E. M. Seibel, J. H. Roudebush, H. Wu, Q. Huang, M. N. Ali, H. Ji, and R. J. Cava, Inorg. Chem. **52**, 13605 (2013).

[13] R. Berthelot, W. Schmidt, S. Muir, J. Eilertsen, L. Etienne, A. W. Sleight, and M. A. Subramanian, Inorg. Chem. **51**, 5377 (2012).

[14] N. Rogado, Q. Huang, J. W. Lynn, A. P. Ramirez, D. Huse, and R. J. Cava, Phys. Rev. B **65**, 144443 (2002).

[15] A. Yogi, A. K. Bera, A. Maurya, R. Kulkarni, S. M. Yusuf, A. Hoser, A. A. Tsirlin, and A. Thamizhavel, Phys. Rev. B **95**, 024401 (2017).

[16] A. Yogi, A. K. Bera, A. Maurya, R. Kulkarni, S. M. Yusuf, A. Hoser, A. A. Tsirlin, and A. Thamizhavel, Phys. Rev. B **96**, 059903(E) (2017).

[17] D. Bertrand and H. Kerner-Czeskleba, J. de Phys. **36**, 379 (1975).

[18] S. McAlister and P. Strobel, J. Magn. Magn. Mater. **30**, 340 (1983).

[19] T. Kurumaji, S. Ishiwata, and Y. Tokura, Phys. Rev. B **95**, 045142 (2017).

[20] I. Dzyaloshinsky, J. Phys. Chem. Solids **4**, 241 (1958).

[21] T. Moriya, Phys. Rev. **120**, 91 (1960).

[22] F. Keffer, Phys. Rev. **126**, 896 (1962).

[23] S.-W. Cheong and M. Mostovoy, Nat. Mater. **6**, 13 (2007).

[24] T. Dunn, Trans. Faraday Soc. **57**, 1441 (1961).

[25] A. L. Wysocki, K. D. Belashchenko, and V. P. Antropov, Nat. Phys. **7**, 485 (2011).

[26] J. K. Glasbrenner, I. I. Mazin, H. O. Jeschke, P. J. Hirschfeld, R. M. Fernandes, and R. Valenti, Nat. Phys. **11**, 953 (2015).

[27] L. W. Harriger, H. Q. Luo, M. S. Liu, C. Frost, J. P. Hu, M. R. Norman, and P. Dai, Phys. Rev. B **84**, 054544 (2011).

[28] R. Yu, Z. Wang, P. Goswami, A. H. Nevidomskyy, Q. Si, and E. Abrahams, Phys. Rev. B **86**, 085148 (2012).

[29] P. Bilbao Ergueta and A. H. Nevidomskyy, Phys. Rev. B **92**, 165102 (2015).

[30] P. Bilbao Ergueta, W.-J. Hu, and A. H. Nevidomskyy, Phys. Rev. B **96**, 174403 (2017).

[31] S. Toth and B. Lake, J. Phys.: Condens. Matter **27**, 166002 (2015).

[32] M. Rotter, M. D. Le, A. T. Boothroyd, and J. A. Blanco, J. Phys.: Condens. Matter **24**, 213201 (2012).

[33] P. P. Stavropoulos, D. Pereira, and H.-Y. Kee, Phys. Rev. Lett. **123**, 037203 (2019).

[34] V. I. Anisimov, I. V. Solovyev, M. A. Korotin, M. T. Czyżyk, and G. A. Sawatzky, Phys. Rev. B **48**, 16929 (1993).

[35] G. Kresse and J. Furthmüller, Comput. Mater. Sci. **6**, 15 (1996).

[36] G. Kresse and D. Joubert, Phys. Rev. B **59**, 1758 (1999).

[37] J. P. Perdew, K. Burke, and M. Ernzerhof, Phys. Rev. Lett. **77**, 3865 (1996).

[38] J. M. Luttinger and L. Tisza, Phys. Rev. **70**, 954 (1946).

[39] D. H. Lyons and T. A. Kaplan, Phys. Rev. **120**, 1580 (1960).

[40] B. Gao, T. Chen, X. Wu, M. Flynn, C. Duan, L. Chen, C. Huang, J. Liebman, S. Li, F. Ye *et al.* (private communication).